

# Cell type-specific differential expression in spatial transcriptomics

Dylan M. Cable<sup>1,2,3</sup>, Evan Murray<sup>2</sup>, Vignesh Shanmugam<sup>2,4</sup>,  
Simon Zhang<sup>2</sup>, Michael Diao<sup>1,2</sup>, Haiqi Chen<sup>2</sup>,  
Evan Z. Macosko<sup>2,5</sup>, Rafael A. Irizarry<sup>3,6,\*</sup>, and Fei Chen<sup>2,7,\*</sup>

<sup>1</sup>Department of Electrical Engineering and Computer Science, MIT, Cambridge, MA, 02139

<sup>2</sup>Broad Institute of Harvard and MIT, Cambridge, MA, 02142

<sup>3</sup>Department of Data Sciences, Dana-Farber Cancer Institute, Boston, MA, 02215

<sup>4</sup>Department of Pathology, Brigham and Women's Hospital and Harvard Medical School, Boston MA 02115

<sup>5</sup>Department of Psychiatry, Massachusetts General Hospital, Boston, MA, 02114

<sup>6</sup>Department of Biostatistics, Harvard University, Boston, MA, 02115

<sup>7</sup>Department of Stem Cell and Regenerative Biology, Harvard University, Cambridge MA 02138

\*These authors contributed equally

Correspondence to: [chenf@broadinstitute.org](mailto:chenf@broadinstitute.org), [rafa@ds.dfci.harvard.edu](mailto:rafa@ds.dfci.harvard.edu)

December, 15th 2021

## Abstract

Spatial transcriptomics enables spatially resolved gene expression measurements at near single-cell resolution. There is a pressing need for computational tools to enable the detection of genes that are differentially expressed across tissue context for cell types of interest. However, changes in cell type composition across space and the fact that measurement units often detect transcripts from more than one cell type introduce complex statistical challenges. Here, we introduce a statistical method, Generalized Linear Admixture Models for Differential Expression (GLAMDE), that estimates cell type-specific patterns of differential gene expression while accounting for localization of other cell types. By using general log-linear models, we provide a unified framework for defining and identifying gene expression changes for a wide-range of relevant contexts: changes due to pathology, anatomical regions, physical proximity to specific cell types, and cellular microenvironment. Furthermore, our approach enables statistical inference across multiple samples and replicates when such data is available. We demonstrate, through simulations and validation experiments on Slide-seq and MERFISH datasets, that our approach accurately identifies cell type-specific differential gene expression and provides valid uncertainty quantification. Lastly, we apply our method to characterize spatially-localized tissue changes in the context of disease. In an Alzheimer's mouse model Slide-seq dataset, we identify plaque-dependent patterns of cellular immune activity. We also find a putative interaction between tumor cells and myeloid immune cells in a Slide-seq tumor dataset. We make our GLAMDE method publicly available as part of the open source R package <https://github.com/dmcable/spacexr>.

## Introduction

Spatial transcriptomics technologies profile gene expression in parallel across hundreds or thousands of genes across spatial measurement units, or *pixels* [1–9]. These technologies have the potential to associate gene expression with cellular context such as spatial position, proximity to pathology, or cell-to-cell interactions. Studying gene expression changes, termed *differential expression* (DE), within

42 tissue context has the potential to provide insight into principles of organization of complex tissues  
43 and disorganization in disease and pathology [1, 10–13].

44 Current methods for addressing differential expression in spatial transcriptomics fall into two cate-  
45 gories: nonparametric and parametric methods. Nonparametric differential expression methods [14–17]  
46 do not use constrained hypotheses about gene expression patterns, but rather fit general smooth spatial  
47 patterns of gene expression. Some of these approaches do not take cell types into account [14, 15], while  
48 others operate on individual cell types [17]. Discovering non-parametric differential gene expression  
49 can be advantageous in order to generate diverse exploratory hypotheses. However, if covariates are  
50 available, for example predefined anatomical regions, parametric approaches increase statistical power  
51 substantially and provide directly interpretable parameter estimates. Specific differential expression  
52 problems have been addressed with ad-hoc solutions such as detecting gene expression dependent on  
53 cell-to-cell colocalization [18] or anatomical regions [10, 19], but no general parametric framework is  
54 currently available. In contrast, general parametric frameworks have been widely applied across bulk  
55 and single-cell RNA-sequencing (scRNA-seq) to test for differences in gene expression across cell type,  
56 disease state, and developmental state, among other problems [20–22]. Furthermore, although multi-  
57 sample, multi-replicate differential expression methods exist for bulk and single-cell RNA-seq [20–22],  
58 no statistical framework accounting for technical and biological variation [23] across samples and repli-  
59 cates has been established for the spatial setting.

60 An important challenge unaddressed by current spatial transcriptomics DE methods is accounting  
61 for observations generated from cell type mixtures. In particular, sequencing-based, RNA-capture  
62 spatial transcriptomics technologies, such as Visium [7], DBiT-seq [6], GeoMx [8], and Slide-seq [1, 2],  
63 can capture multiple cell types on individual measurement pixels. The presence of cell type mixtures  
64 complicates the estimation of *cell type-specific differential expression* (i.e. DE within a cell type of  
65 interest) because different cell types have different gene expression profiles, independent of spatial  
66 location [24, 25]. Although imaging-based spatial transcriptomics technologies, such as MERFISH [3],  
67 seqFISH [5], ExSeq [9], and STARmap [4], have the potential to achieve single cell resolution, these  
68 technologies may encounter mixing or contamination across cell types due to diffusion or imperfect  
69 cellular segmentation [26]. Several methods [24, 27, 28] have been developed to identify cell type  
70 proportions in spatial transcriptomics datasets. However, at present no method accounts for cell type  
71 proportions in differential expression analysis. Here, we demonstrate how not accounting for cell type  
72 proportions leads to biased estimates of differential gene expression due to confounding caused by cell  
73 type proportion changes or contamination from other cell types.

74 In this work we introduce Generalized Linear Admixture Models for Differential Expression (GLAMDE),  
75 a general parametric statistical method that estimates cell type-specific differential expression in the  
76 context of cell type mixtures. The first step is to estimate cell type proportions on each pixel using a  
77 cell type-annotated single-cell RNA-seq (scRNA-seq) reference [24]. Next, we fit a parametric model,  
78 using predefined covariates such as spatial location or cellular microenvironment, that accounts for cell  
79 type differences to obtain cell type-specific differential expression estimates and corresponding stan-  
80 dard errors. The model accounts for sampling noise, gene-specific overdispersion, multiple hypothesis  
81 testing, and platform effects between the scRNA-seq reference and the spatial data. Furthermore, when  
82 multiple experimental samples are available, the GLAMDE model permits statistical inference across  
83 multiple samples and/or replicates to achieve more stable estimates of population-level differential  
84 gene expression.

85 Using simulated and real spatial transcriptomics data, we show GLAMDE accurately estimates cell  
86 type-specific differential expression while controlling for changes in cell type proportions and contam-  
87 ination from other cell types. We also demonstrate how cell type mixture modelling increases power,  
88 especially when single cell type measurements are rare. Furthermore, on Slide-seq and MERFISH  
89 datasets, we demonstrate how GLAMDE’s general parametric framework enables testing differential  
90 gene expression for diverse hypotheses including spatial position or anatomical regions [29], cell-to-cell  
91 interactions, cellular environment, or proximity to pathology. By associating gene expression changes  
92 with particular cell types, we use GLAMDE to systematically link gene expression changes to cellular  
93 context in pathological tissues such as Alzheimer’s disease and cancer.

## 94 Results

### 95 Generalized Linear Admixture Models for Differential Expression learns cell 96 type-specific differential gene expression in the context of spatial transcrip- 97 tomics cell type mixtures

Here, we develop Generalized Linear Admixture Models for Differential Expression (GLAMDE), a statistical method for determining differential expression (DE) in spatial transcriptomics datasets (Figure 1a). GLAMDE inputs one or more experimental samples of spatial transcriptomics data, consisting of  $Y_{i,j,g}$  as the observed RNA counts for pixel  $i$ , gene  $j$ , and experimental sample  $g$ . We then assume Poisson sampling so that,

$$Y_{i,j,g} \mid \lambda_{i,j,g} \sim \text{Poisson}(N_{i,g}\lambda_{i,j,g}), \quad (1)$$

with  $\lambda_{i,j,g}$  the expected count and  $N_{i,g}$  the total transcript count (e.g. total UMIs) for pixel  $i$  on experimental sample  $g$ . Accounting for platform effects and other sources of technical and natural variability, we assume  $\lambda_{i,j,g}$  is a mixture of  $K$  cell type expression profiles, defined by,

$$\log(\lambda_{i,j,g}) = \log\left(\sum_{k=1}^K \beta_{i,k,g} \mu_{i,k,j,g}\right) + \gamma_{j,g} + \varepsilon_{i,j,g}, \quad (2)$$

98 with  $\mu_{i,k,j,g}$  the cell type-specific expected gene expression rate for pixel  $i$ , gene  $j$ , experimental sample  
99  $g$ , and cell type  $k$ ;  $\beta_{i,k,g}$  the proportion of cell type  $k$  contained in pixel  $i$  for experimental sample  $g$ ;  
100  $\gamma_{j,g}$  a gene-specific random effect that accounts for platform variability; and  $\varepsilon_{i,j,g}$  a random effect to  
101 account for gene-specific overdispersion.

To account for cell type-specific differential expression, we model across pixel locations the log of the cell type-specific profiles  $\mu_{i,k,j,g}$  as a linear combination of  $L$  covariates used to explain differential expression. Specifically, we assume that,

$$\log(\mu_{i,k,j,g}) = \alpha_{0,k,j,g} + \sum_{\ell=1}^L x_{i,\ell,g} \alpha_{\ell,k,j,g}. \quad (3)$$

102 Here,  $\alpha_{0,k,j,g}$  represents the intercept term for gene  $j$  and cell type  $k$  in sample  $g$ , and  $x_{i,\ell,g}$  represents  
103 the  $\ell$ 'th *covariate*, evaluated at pixel  $i$  in sample  $g$ . Similarly as in linear and generalized linear  
104 models [30],  $x$ , also called the *design matrix*, represents predefined covariate(s) that explain differential  
105 expression, and the corresponding coefficient(s)  $\alpha_{\ell,k,j,g}$  each represent the DE effect size of covariate  $\ell$   
106 for gene  $j$  in cell type  $k$  for sample  $g$ .

107 With this general framework we can describe any type of differential expression that can be pa-  
108 rameterized with a log-linear model. Examples include (Figure 1b):

- 109 1. Differential expression between multiple regions. In this case, the tissue is manually segmented  
110 into multiple regions (e.g. nodular and anterior cerebellum, Figure 3). Design matrix  $x$  contains  
111 discrete categorical indicator variables representing membership in 2 or greater regions.
- 112 2. Differential expression due to cellular environment or state (special case of (1)). Pixels are  
113 discretely classified into local environments based on the surrounding cells (e.g. stages in the  
114 testes Slide-seq dataset, Figure 4).
- 115 3. Differential expression as a function of distance to a specific anatomical feature. In this case,  
116  $x$  is defined as the spatial position or distance to some feature (e.g. distance to midline in the  
117 hypothalamus MERFISH dataset, Figure 4).
- 118 4. Cell-to-cell interactions. In this case, we define a cell-to-cell interaction as differential expression  
119 within one cell type ( $A$ ) due to co-localization with a second cell type ( $B$ ) (e.g. immune cell  
120 density in cancer, Figure 5). For this problem,  $x$  is the continuous density of cell type  $B$ .

- 121 5. Proximity to pathology. Similar to (4), except covariate  $x$  represents density of a pathological  
122 feature (e.g. Alzheimer’s  $A\beta$  plaque, Figure 4), rather than cell type density.
- 123 6. General spatial patterns (termed *nonparametric*). In this case, we define design matrix  $x$  to  
124 be smooth basis functions [31], where linear combinations of these basis functions represent the  
125 overall smooth gene expression function and can accommodate any smooth spatial pattern.

126 To estimate this complex model with a computationally tractable algorithm, we note that the gene  
127 expression variability across cell types is large enough that, in the first step, we can assume  $\mu_{i,k,j,g}$   
128 does not vary with  $i$  and  $g$  and estimate  $\beta$  using a previously published algorithm [24]. Here, some  
129 pixels are identified as single cell types while others as mixtures of multiple cell types. Fixing the  
130  $\beta$  estimates, we next use maximum likelihood estimation to estimate the cell type-specific DE coef-  
131 ficients  $\alpha$  with corresponding standard errors, allowing for false discovery rate-controlled hypotheses  
132 testing (see *Methods* for details). Lastly, GLAMDE performs statistical inference across multiple repli-  
133 cates and/or samples, accounting for biological and technical variation across replicates, to estimate  
134 consensus population-level differential expression (*Methods*, Supplementary Figure 1).

135 Because ground truth cell type-specific DE is unknown in spatial transcriptomics data, we first  
136 benchmarked GLAMDE’s performance on a simulated spatial transcriptomics dataset in which gene  
137 expression varied across two regions. Considering the challenging situation where two cell types, termed  
138 *cell type A* and *cell type B*, are colocalized on pixels within a tissue, we simulated, using a single-nucleus  
139 RNA-seq cerebellum dataset, spatial transcriptomics mixture pixels with known proportions of single  
140 cells from two cell types known to spatially colocalize [32] (*Methods*, Figure 2a). Across two spatially-  
141 defined regions, we varied both the true cell type-specific gene expression of cell types A and B as well  
142 as the average cell type proportions of cell types A and B (Figure 2a, Supplementary Figure 2). We  
143 compared GLAMDE against three alternative methods (see *Methods* for details): *Bulk*, bulk differential  
144 expression (ignoring cell type); *Single*, single cell differential expression that approximates each cell  
145 type mixture as a single cell type; and *Decompose*, a method that decomposes mixtures into single  
146 cell types prior to computing differential expression. By varying cell type frequencies between the two  
147 regions without introducing differential expression, we observed that GLAMDE correctly attributes  
148 gene expression differences across regions to differences in cell type proportions rather than spatial  
149 differential expression (Figure 2b, Supplementary Figure 2); in contrast, the Bulk method incorrectly  
150 predicts spatial differential expression since it does not control for differences of cell type proportions  
151 across regions.

152 Next, we simulated cell type-specific differential expression (DE) by varying the differential expres-  
153 sion in cell type A while keeping cell type B constant across regions. Background DE in cell type A  
154 contaminated estimates of differential expression in cell type B for all three alternatives models Bulk,  
155 Decompose, and Single (Figure 2c, Supplementary Figure 2). In contrast, GLAMDE’s joint model of  
156 cell type mixtures and cell type-specific differential expression correctly identified differential expression  
157 in cell type A, but not cell type B. Next, we verified that, under the null hypothesis of zero differential  
158 expression, GLAMDE’s false positive rate was accurately controlled, standard errors were accurately  
159 estimated, and confidence intervals contained the ground truth DE (Figure 2d, Supplementary Fig-  
160 ure 2). Finally, when nonzero differential expression was simulated, GLAMDE achieved unbiased  
161 estimation of cell type-specific differential expression (Figure 2e). We also found that the power of  
162 GLAMDE depends on gene expression level, number of cells, and differential expression magnitude  
163 (Supplementary Figure 2). Thus, our simulations validate GLAMDE’s ability to accurately estimate  
164 and test for cell type-specific differential expression in the cases of asymmetric cell type proportions  
165 and contamination from other cell types.

## 166 **GLAMDE accurately identifies cell type-specific differential expression in** 167 **spatial transcriptomics data**

168 To validate GLAMDE’s ability to discover cell type-specific differential expression on spatial transcrip-  
169 tomics data, we collected Slide-seqV2 data [2] (including one replicate sourced from a prior study [24])



170 for three cerebellum replicates. We identified a spatial map of cell types (Figure 3a), previously shown  
171 to correspond to known cerebellum spatial architecture [24]. We used discrete localization in the anterior  
172 lobule or nodulus regions (Figure 3b), a known axis of spatial gene expression variation within the  
173 cerebellum [32], as a covariate and estimated cell type-specific DE across regions using GLAMDE (Figure  
174 3c, Supplementary Figure 3, Supplementary Table 1). As experimental validation, we performed  
175 hybridization chain reaction (HCR) on four genes identified to be differentially expressed in specific  
176 cell types, and we observed high correspondence between GLAMDE’s estimates of cell type-specific  
177 differential expression and DE measurements from HCR data (Figure 3d,  $R^2 = 0.89$ ). For example,  
178 we examined *Aldoc* and *Plcb4*, two genes expressed in both Purkinje and Bergmann cell types, which  
179 are known to spatially colocalize in the cerebellum and appear as mixtures on Slide-seq pixels [24].  
180 GLAMDE determined that both *Aldoc* ( $\log_2$ -fold-change =  $-4.24$ ,  $p < 10^{-8}$ ) and *Plcb4* ( $\log_2$ -fold-  
181 change =  $1.93$ ,  $p < 10^{-8}$ ) were differentially expressed in the Purkinje cell type, but not the Bergmann  
182 cell type. Similarly, HCR images of *Aldoc* and *Plcb4* showed substantial differential expression within  
183 Purkinje cells across the nodulus and anterior lobule, whereas expression within Bergmann cells was  
184 relatively even across regions (Figure 3d–e). We conclude that GLAMDE can successfully identify cell  
185 type-specific spatial differential expression in spatial transcriptomics tissues, even when multiple cell  
186 types are spatially colocalized.

## 187 **GLAMDE solves a diverse array of differential gene expression problems in** 188 **spatial transcriptomics**

189 We next explored the effect of discrete cellular microenvironments on cell type-specific DE in the mouse  
190 testes Slide-seq dataset [12]. GLAMDE’s testes principal cell type assignments (Figure 4a) revealed  
191 tubular structures corresponding to cross-sectional sampling of seminiferous tubules. Individual tubules  
192 have distinct stages of spermatogonia development, grouped into four classes of stages I–III, IV–VI,  
193 VII–VIII, and IX–XII, which were determined from the prior testes Slide-seq study using tubule-  
194 level gene expression clustering [12] (Figure 4b). Given that each tubule stage represents a distinct  
195 microenvironment along the testes developmental trajectory, we applied GLAMDE to identify genes  
196 that were differentially expressed, for each cell type, across tubule stages (Supplementary Table 2).  
197 Furthermore, GLAMDE identified genes expressed in a single tubule stage within a single cell type  
198 (Figure 4c) which are known drivers of cellular development across stages [12]. For instance, the gene  
199 *Tnp1* was identified by GLAMDE as upregulated in the IX–XII stage within the elongating spermatid  
200 (ES) cell type, in agreement with the known biological role of *Tnp1* in nuclear remodeling of elongating  
201 spermatids at the late tubule stage [33] (Supplementary Figure 4). After identifying stage-specific genes  
202 within each cell type, we additionally found that a majority of GLAMDE-identified stage-specific genes  
203 followed cyclic patterns across stages, consistent with previously-characterized cyclic gene regulation  
204 in what is referred to as the seminiferous epithelial cycle [34] (Supplementary Figure 4).

205 Next, we evaluated GLAMDE’s ability to identify DE for cell types that primarily appear as  
206 mixtures with other cell types, particularly the spermatocyte (SPC) cell type. According to GLAMDE  
207 cell type assignments, SPC frequently co-mixes with the ES and round spermatid (RS) cell types,  
208 consistent with the known colocalization of spermatocytes with spermatids from previous histological  
209 studies [35] (Supplementary Figure 4). Due to GLAMDE’s ability to learn DE from cell type mixtures,  
210 GLAMDE obtained increased power for identifying differentially expressed genes compared to a DE  
211 method that only uses single cell type pixels (see *Supplementary Methods* for details, Supplementary  
212 Figure 4), especially for spermatocyte cell type (217 significant SPC DE genes discovered by GLAMDE  
213 vs. 1 DE gene for the single cell method). In order to validate GLAMDE’s determination that *Prss40*  
214 ( $\log_2$ -fold-change =  $1.72$ ,  $p = 8 \cdot 10^{-5}$ ) and *Snx3* ( $\log_2$ -fold-change =  $1.17$ ,  $p < 10^{-8}$ ) were differentially  
215 expressed, between stage I–III and stage IX–XII, specifically in the SPC cell type, we compared the  
216 average gene expression for three categories of testes pixels: pixels containing spermatid cell types,  
217 but not SPC (called S+, SPC-); pixels containing both spermatid and SPC cell types (S+, SPC+);  
218 and pixels containing SPC but not spermatids (S-, SPC+) (Figure 4d). For both genes, differential  
219 expression across stages was not observed in (S+, SPC-) pixels, indicating that the spermatid cell types

220 do not exhibit DE. However, (S+, SPC+) pixels are significantly differentially expressed across stages,  
221 enabling GLAMDE to infer DE specifically in the SPC cell type. On the other hand, (S-, SPC+)  
222 pixels, which include SPC single cells, are not significantly differentially expressed across regions, due  
223 to their low sample size. Therefore, GLAMDE’s ability to handle cell type mixtures uniquely enables  
224 the discovery of differential expression, even in cell types that only appear as mixtures with other cell  
225 types.

## 226 **GLAMDE identifies spatial gene expression changes in imaging-based technologies**

227 Next, we demonstrated the utility of GLAMDE on an imaging-based spatial transcriptomics dataset  
228 (i.e. MERFISH) which achieves closer to single-cell resolution compared to capture-based spatial tran-  
229 scriptomics technologies (e.g. Slide-seq, Visium), which contain frequent cell type mixtures [24]. To  
230 do so, we applied GLAMDE to a MERFISH dataset collected in the mouse hypothalamus. During  
231 development, hypothalamic progenitors create radial projections out from the hypothalamic midline,  
232 which are used as scaffolds for the migration of differentiating daughter cells [36]. Thus, we investigated  
233 radial distance to the hypothalamus midline as a predictor of differential expression in hypothalamus  
234 cell types. First, we assigned cell types and found them to be consistent with the prior MERFISH hy-  
235 pothalamus study [11] (Figure 4e). Although GLAMDE mostly assigned single cell types to MERFISH  
236 pixels, a non-negligible proportion (12.6% double cell type pixels out of  $n = 3790$  total single and dou-  
237 ble cell type pixels) of pixels were assigned as mixtures of more than one cell type. Next, we computed  
238 midline distance as a covariate for GLAMDE (Figure 4f), and we next detected genes in hypothalamus  
239 excitatory, inhibitory, and mature oligodendrocyte cell types whose expression depended either linearly  
240 or quadratically on distance from the midline (Figure 4g, Supplementary Table 3–4). For instance,  
241 *Slc18a2* (Figure 4h), identified by GLAMDE as differentially upregulated within inhibitory neurons  
242 near the midline ( $\log_2$ -fold-change = 6.14,  $p < 10^{-8}$ ), is required for dopaminergic function in certain  
243 inhibitory neuronal subtypes [37], which are known to localize near the hypothalamus midline [11].

## 244 **GLAMDE enables discovery of $A\beta$ plaque-dependent cell type-specific differential ex- 245 pression in Alzheimer’s disease**

246 We next explored the use of pathological staining, in particular  $A\beta$  plaques, as a continuous covariate  
247 for cell type-specific gene expression changes. To do so, we performed Slide-seqV2 on the hippocampal  
248 region of a genetic mouse model of amyloidosis in Alzheimer’s disease (AD) [38] (J20,  $n = 4$  slices,  
249 *Methods*). GLAMDE identified spatial maps of cell types (Figure 4i) which were consistent with past  
250 characterizations of hippocampus cellular localization [24]. We collected paired  $A\beta$  plaque staining  
251 images (Anti-Human  $A\beta$  Mouse IgG antibody, *Methods*) to quantify the  $A\beta$  plaque density to use as  
252 a covariate for GLAMDE (Figure 4j, Supplementary Figure 5). We then used GLAMDE to identify  
253 genes whose expression depended in a cell type-specific manner on  $A\beta$  plaque density (Figure 4k,  
254 Supplementary Table 5). For instance, we found that *Gfap* was enriched in astrocytes colocalizing  
255 with  $A\beta$  plaque (Figure 4l, Supplementary Figure 5,  $\log_2$ -fold-change = 1.35,  $p < 10^{-8}$ ), a result  
256 corroborated by studies that have established the role of *Gfap* in attenuating the proliferation of  $A\beta$   
257 plaques [39]. GLAMDE additionally discovered upregulation in astrocytes of the *C4b* complement  
258 gene ( $\log_2$ -fold-change = .85,  $p = 1 \cdot 10^{-4}$ ), which is involved in plaque-associated synaptic pruning in  
259 Alzheimer’s disease [40–42]. Moreover, several cathepsin proteases including *Ctsb* ( $\log_2$ -fold-change =  
260 1.65,  $p < 10^{-8}$ ), *Ctsd* ( $\log_2$ -fold-change = 1.30,  $p < 10^{-8}$ ) *Ctsl* ( $\log_2$ -fold-change = 1.96,  $p = 4 \cdot 10^{-6}$ ),  
261 and *Ctsz* ( $\log_2$ -fold-change = 1.11,  $p = 3 \cdot 10^{-4}$ ) were determined to be differentially upregulated  
262 in microglia around plaque, consistent with prior evidence that cathepsins are involved with amyloid  
263 degradation in Alzheimer’s disease [43] (Supplementary Figure 5). In microglia, we also identified  
264 known homeostatic microglia markers [44–46] including *P2ry12* ( $\log_2$ -fold-change =  $-1.33$ ,  $p < 10^{-8}$ )  
265 and *Cx3cr1* ( $\log_2$ -fold-change =  $-0.68$ ,  $p = 3 \cdot 10^{-4}$ ) as downregulated in the presence of plaque. *Apoe*,  
266 which is known to have  $A\beta$  plaque-dependent upregulation within microglia [47], was also detected  
267 as significant ( $\log_2$ -fold-change = 1.58,  $p < 10^{-8}$ ), although it did not pass default GLAMDE gene

268 filters (*Methods*) due to its four-fold higher expression in astrocytes than microglia. Finally, the anti-  
269 inflammatory gene *Grn* was determined by GLAMDE to be upregulated in microglia near plaque  
270 ( $\log_2$ -fold-change = 0.79,  $p = 6 \cdot 10^{-4}$ ), consistent with prior knowledge [48].

## 271 **GLAMDE discovers tumor-immune signaling in a mouse tumor model**

272 Finally, we applied GLAMDE to identify genes with cell type-specific spatial differential expression in  
273 a Slide-seq dataset of a *Kras*<sup>G12D/+</sup> *Trp53*<sup>-/-</sup> (KP) mouse tumor model [49, 50], where we analyzed a  
274 single metastatic lung adenocarcinoma tumor deposit in the liver. We first used GLAMDE to generate  
275 a spatial map of cell types and found several cell types within the tumor, including both tumor  
276 cells and myeloid cells (Figure 5a). Next, we ran GLAMDE nonparametrically to discover arbitrary  
277 smooth gene expression patterns (see *Supplementary Methods* for details, Supplementary Table 6). For  
278 gene expression within the tumor cell type, this procedure identified three categories of genes: genes  
279 with variable expression purely due to sampling noise rather than biology, genes exhibiting biological  
280 variation partially explained by the spatial GLAMDE model, and genes exhibiting biological variation  
281 not explained by the spatial model (Figure 5b, Supplementary Figure 6). We then hierarchically  
282 clustered the GLAMDE fitted spatial patterns of significant differentially expressed genes within the  
283 tumor cell type into seven clusters with distinct spatial patterns (Figure 5c, Supplementary Figure  
284 6). We tested each cluster for gene set enrichment (see *Supplementary Methods* for details), and we  
285 identified the *Myc* targets gene set as enriched in cluster 5 (7 out of 12 genes,  $p = 2 \cdot 10^{-4}$ , two-  
286 sided binomial test, Supplementary Table 7, 1 significant gene set out of 50 tested), a cluster with a  
287 spatial pattern of overexpression at the tumor boundary (Figure 5d). High expression of *Myc* target  
288 genes is potentially indicative of an increased rate of proliferation [51] at the boundary, which has  
289 been previously proposed as a correlate of tumor severity [52]. For example, the *Myc* target found  
290 to have the most differential upregulation at the tumor boundary, *Kpnb1* (Supplementary Figure 6,  
291  $p = 1 \cdot 10^{-5}$ ), has been previously been identified as an oncogene that drives cell proliferation and  
292 suppresses apoptosis [53, 54].

293 Given the substantial variation in tumor cell spatial expression patterns, we next tested if such  
294 variability could be explained by cell-to-cell interactions with immune cells, which have been shown to  
295 influence tumor cell behavior in prior studies [55–57]. Using myeloid cell type density as the GLAMDE  
296 covariate (Figure 5e), GLAMDE identified genes with immune cell density-dependent cell type-specific  
297 differential expression (Figure 5f, Supplementary Table 8), including several genes that were also  
298 discovered by our nonparametric procedure (Supplementary Figure 6). One of the genes with the  
299 largest effects, *Ccl2* ( $\log_2$ -fold-change = 1.74,  $p < 10^{-8}$ ), is a chemotactic signaling molecule known  
300 to attract myeloid cells [58, 59]. Furthermore, we tested GLAMDE’s DE gene estimates for aggregate  
301 effects across gene sets and found that the epithelial-mesenchymal transition (EMT) pathway was  
302 significantly upregulated on average near immune cells (Figure 5f, Supplementary Figure 6,  $p = 0.0011$ ,  
303 permutation test (see *Methods*), 1 significant gene set out of 50 tested, Supplementary Table 7).  
304 GLAMDE additionally identified *Nfkb1* as upregulated in tumor cells in immune-rich regions ( $\log_2$ -  
305 fold-change = 1.10,  $p = 1 \cdot 10^{-5}$ ), a gene that has been previously implicated in positively regulating the  
306 EMT pathway of tumor cells [60, 61]. Moreover, the majority of tumor cells exhibiting a mesenchymal  
307 phenotype were located in immune-rich regions (Figure 5g). Furthermore, morphological analysis and  
308 annotation of an hematoxylin and eosin (H&E) stained adjacent section of the tumor demonstrated a  
309 clear increase in the number of spindle-shaped tumor cells relative to polygonal-shaped tumor cells in  
310 the immune rich-areas (Figure 5h). The collective morphological and gene expression changes suggest  
311 a role for the immune microenvironment in influencing the epithelial-mesenchymal transition in this  
312 tumor model [62]. Therefore, both exploratory nonparametric GLAMDE and more targeted immune  
313 cell-dependent DE reveal biologically-relevant signatures of differential gene expression.

## 314 Discussion

315 Elucidating spatial sources of differential gene expression is a critical challenge for understanding  
316 biological mechanisms and disease with spatial transcriptomics. Here we introduced GLAMDE, a  
317 statistical method to detect cell type-specific DE in spatial transcriptomics datasets. GLAMDE takes  
318 as input one or more biologically-relevant covariates, such as spatial position or cell type colocalization,  
319 and identifies genes, for each cell type, that significantly change their expression as a function of  
320 these covariates. Tested on simulated spatial transcriptomics data, GLAMDE obtained unbiased  
321 estimation of cell type-specific differential gene expression with a calibrated false positive rate, while  
322 other methods were biased from changes in cell type proportion or contamination from other cell  
323 types. In the cerebellum, we additionally used HCR experiments to validate GLAMDE's ability to  
324 identify cell type-specific DE across regions. We further applied GLAMDE to a detect differential  
325 expression depending on tubular microenvironment in the testes, midline distance in the MERFISH  
326 hypothalamus, and  $A\beta$  plaque density in the Alzheimer's model hippocampus. Finally, we applied  
327 both nonparametric and parametric GLAMDE procedures in a mouse tumor model to discover an  
328 increase in tumor cells undergoing EMT transition in immune-rich regions.

329 Several studies have established the importance of accounting for cell type mixtures in assigning  
330 cell types in spatial transcriptomics data [24,27,28]. However, it remains a challenge to incorporate cell  
331 type proportions into models of cell type-specific spatial differential gene expression. GLAMDE enables  
332 such cell type-specific DE discovery by creating a statistical model of cell type-specific differential gene  
333 expression in the presence of cell type mixtures. In this study, we demonstrated how other potential  
334 solutions, such as bulk DE, approximation as single cell types, and decomposition into single cell types  
335 can be confounded by cell type proportion changes and contamination from other cell types. GLAMDE  
336 solves these issues by controlling for cell type proportions and jointly considering differential expression  
337 within each cell type. Even in imaging-based spatial transcriptomics methods such as MERFISH that  
338 mostly contain single cell type pixels, we detected some pixels with cell type mixtures, indicating  
339 potential diffusion or imperfect cell segmentation [26]. To control for cell type proportions in DE  
340 analysis, GLAMDE can estimate cell types directly or import cell type proportions from any cell type  
341 mixture identification method [24,27,28].

342 GLAMDE provides a unified framework for detecting biologically-relevant differential expression  
343 in spatial transcriptomics tissues along diverse array of axes including spatial distance, proximity to  
344 pathology, cellular microenvironment, and cell-to-cell interactions. In settings without prior biological  
345 hypotheses, GLAMDE may be run nonparametrically to discover general cell type-specific spatial  
346 gene expression patterns. When using problem-specific knowledge to generate biologically-relevant  
347 DE predictors, parametric GLAMDE efficiently detects DE genes along the parametric hypothesis  
348 axes. GLAMDE can also be used to test among multiple models of differential expression, such as the  
349 linear and quadratic models applied to the hypothalamus dataset. GLAMDE can also utilize multiple  
350 covariates in a joint model of gene expression, such as spatial position and cell type colocalization,  
351 although more complicated models require more data to fit accurately. Beyond individual samples,  
352 GLAMDE can also perform differential expression statistical inference at the population level across  
353 multiple replicates or biological samples, including modeling biological and technical variability in  
354 complex multi-sample, multi-replicate experiments. Multi-replicate experiments, though more costly,  
355 produce more robust DE estimates by reducing spurious discoveries of DE on single replicates.

356 One challenge for GLAMDE is obtaining sufficient DE detection statistical power, which we ob-  
357 served can be hindered by low gene expression counts, small pixel number, or rare cell types. An  
358 advantage of GLAMDE is that it increases its statistical power by including cell type mixture pixels in  
359 its model. Ongoing technical improvements in spatial transcriptomics technologies [2] such as increased  
360 gene expression counts, higher spatial resolution, and increased pixel number, have the potential to  
361 dramatically increase the discovery rate of GLAMDE. Another limitation of GLAMDE is the require-  
362 ment of an annotated single-cell reference for reference-based identification of cell types in the cell  
363 type assignment step. Although single-cell atlases are increasingly available for biological tissues, they  
364 may contain missing cell types or substantial platform effects [24], and certain spatial transcriptomics



365 tissues may lack a corresponding single-cell reference.

366 We envision GLAMDE to be particularly powerful in the context of bridging cell type-specific gene  
367 expression changes in pathology. Here, we demonstrate this in two contexts: one, wherein we leverage  
368 histological features ( $A\beta$  plaques) as a covariate, and two, wherein we nominate tumor-immune inter-  
369 actions as a covariate. In the first, prior Alzheimer’s disease (AD) studies have discovered candidate  
370 genes for disease-relevance through GWAS [63], bulk RNA and protein differences between AD and  
371 control samples [64], and single cell expression differences of disease associated cellular subtypes [41].  
372 Here, with GLAMDE, we identify many genes previously identified by these methods including *Gfap*  
373 in astrocytes [39] and *ApoE* in microglia [47]; furthermore, we take known disease-level associations  
374 a step further towards mechanistic understanding by directly associating spatial plaque localization  
375 with cell type-specific differential expression. For example, prior studies have established an associ-  
376 ation between complement pathway activation in plaque-dense areas with synaptic pruning [40] and  
377 neuronal degeneration [41] leading to cognitive decline. Using GLAMDE we provide evidence for the  
378 upregulation of complement protein *C4b* specifically within plaque-localized astrocytes [65]. Thus,  
379 amyloid plaques may trigger a cytokine-dependent signaling cascade that stimulates the expression  
380 of complement genes in astrocytes, as supported by prior studies [42]. In contrast to *C4b* upregula-  
381 tion, homeostatic microglia marker *P2ry12*, discovered by GLAMDE to be negatively plaque-associated  
382 within microglia, has been shown to be downregulated in microglia in Alzheimer’s disease (AD), a phe-  
383 nomena associated with neuronal cell loss [44]. *P2ry12* is involved in early stage nucleotide-dependent  
384 activation of microglia and is downregulated in later stages of activated microglia [46]. We hypothesize  
385 that plaque-dense areas in AD trigger microglia activation which downregulates homeostatic microglia  
386 genes such as *P2ry12*. Lastly, the granulins gene (*Grn*), discovered by GLAMDE as upregulated in  
387 microglia near plaques, is an anti-inflammatory gene that attenuates microglia activation [66]. It has  
388 been shown to be upregulated in plaque-localized microglia in AD [48] and to potentially have a role in  
389 reducing plaque deposition and cognitive pathological effects in AD [67] and other pathological protein  
390 aggregates [68].

391 Second, GLAMDE has the potential to elucidate tissue interactions driving system-level behavior  
392 in complex tissues. For example, recent studies have characterized cell-to-cell interactions of immune  
393 cells influencing the behavior of tumor cells [55–57]. Consistent with these studies, on a Slide-seq  
394 dataset of a mouse tumor model, GLAMDE identified several genes whose expression within tumor  
395 cells was upregulated near myeloid immune cells. We postulate that the tumor cells and myeloid cells  
396 are involved in a synergistic feedback loop, driven by cell-to-cell signaling. For example, *Ccl2*, found  
397 by GLAMDE to be upregulated in immune-adjacent tumor cells, is known to chemotactically recruit  
398 myeloid cells and to induce pro-tumorigenic behavior, including growth, angiogenesis, and metastasis,  
399 in myeloid cells [58, 59]. Another synergistic immune-tumor interaction identified by GLAMDE is the  
400 myeloid-associated upregulation of the epithelial-mesenchymal transition (EMT) pathway, known to  
401 be involved in tumor development and metastasis [62]. Although GLAMDE established an association  
402 between immune cell colocalization and mesenchymal-like tumor cell state, conclusive establishment of  
403 mechanism of causation requires future experimentation. Among other hypotheses, it is plausible that  
404 myeloid cells induce tumor cells to undergo the EMT transition, potentially through the *NF- $\kappa$ B* (also  
405 identified as upregulated by GLAMDE) signaling pathway, as supported by other studies [55–57, 62].  
406 Future work is necessary to characterize this phenomena across a broader cohort of samples and to  
407 establish specific molecular mechanisms. Overall, these results highlight the power of combining the  
408 GLAMDE framework with pathological measurements to understand cell type-specific responses to  
409 disease and injury. We envision GLAMDE as a powerful framework for the systematic study of the  
410 impacts of spatial and environmental context on cellular gene expression in spatial transcriptomics  
411 data.



## 412 Methods

### 413 GLAMDE model

414 Here, we describe Generalized Linear Admixture Models for Differential Expression (GLAMDE), a  
415 statistical method for identifying differential expression (DE) in spatial transcriptomics data. Please  
416 first refer to the overall definition of the GLAMDE model in equations (1), (2), and (3). Prior to fitting  
417 GLAMDE, the *design matrix*  $x$  is predefined to contain *covariates*, variables on which gene expression  
418 is hypothesized to depend such as spatial position or cellular microenvironment. Recall that  $x_{i,\ell,g}$   
419 represents the  $\ell$ 'th covariate, evaluated at pixel  $i$  in experimental sample  $g$ . For each covariate  $x_{\cdot,\ell,g}$ ,  
420 there is a corresponding coefficient  $\alpha_{\ell,k,j,g}$ , representing a gene expression change across pixels per  
421 unit change of  $x_{\cdot,\ell,g}$  within cell type  $k$  of experimental sample  $g$ . Next, recall from (2) random effects  
422  $\gamma_{j,g}$  and  $\varepsilon_{i,j,g}$ , which we assume both follow normal distributions with mean 0 and standard deviations  
423  $\sigma_{\gamma,g}$  and  $\sigma_{\varepsilon,j,g}$ , respectively. We designed the overdispersion magnitude,  $\sigma_{\varepsilon,j,g}$  to depend on gene  $j$   
424 because we found evidence that the overdispersion depends on gene  $j$  (Supplementary Figure 7), and  
425 modeling gene-specific overdispersion is necessary for controlling the false-positive rate of GLAMDE.

426 Due to our finding that genes can exhibit DE in some but not all cell types (see e.g. Figure 3c),  
427 GLAMDE generally does not assume that genes share DE patterns across cell types, allowing for the  
428 discovery of cell type-specific DE. We also developed an option where DE can be assumed to be shared  
429 across cell types (*Supplementary Methods*). We note that GLAMDE can be thought of as a modification  
430 of the generalized linear model (GLM) [30] in which each cell type follows a log-linear model before  
431 an admixture of all cell types is observed. As a result, we term our model as a Generalized Linear  
432 Admixture Model (GLAM). See *Fitting the GLAMDE model* and *Hypothesis testing* for GLAMDE  
433 model fitting and hypothesis testing, respectively.

### 434 Parameterization of the design matrix

435 For specific construction of design matrix  $x$  for each dataset, see *Cell type estimation and construction*  
436 *of covariates*. Recall the specific examples of design matrix  $x$  presented in Figure 1b. In general, we  
437 note that  $x$  can take on the following numerical forms:

- 438 1. Indicator variable. In this case,  $x_{i,\ell,g}$  is always either 0 or 1. This represents differential expression  
439 due to membership within a certain spatially-defined pixel set of interest. The coefficient  $\alpha_{k,j,g}$   
440 is interpreted as the log-ratio of gene expression between the two sets for cell type  $k$  and gene  $j$   
441 in experimental sample  $g$ .
- 442 2. Continuous variable. In this case,  $x_{i,\ell,g}$  can take on continuous values representing, for example,  
443 distance from some feature or density of some element. The coefficient  $\alpha_{\ell,k,j,g}$  is interpreted  
444 as the log-fold-change of gene expression per unit change in  $x_{i,\ell,g}$  for cell type  $k$  and gene  $j$  in  
445 sample  $g$ .
- 446 3. Multiple categories. In this case, we use  $x$  to encode membership to finitely many  $L \geq 2$  sets.  
447 For each  $1 \leq \ell \leq L$ , we define  $x_{i,\ell,g}$  to be an indicator variable representing membership in set  
448  $\ell$  for sample  $g$ . To achieve identifiability, the intercept is removed. The coefficient  $\alpha_{\ell,k,j,g}$  is  
449 interpreted as the average gene expression in set  $\ell$  for cell type  $k$  and gene  $j$ . Cell type-specific  
450 differential expression is determined by detecting changes in  $\alpha_{\ell,k,j,g}$  across  $\ell$  within cell type  $k$   
451 and sample  $g$ .
- 452 4. Nonparametric. In this case, we use  $x$  to represent  $L$  smooth basis functions, where linear  
453 combinations of these basis functions represent the overall smooth gene expression function. By  
454 default, we use thin plate spline basis functions, calculated using the `mgcv` package [31].

455 In all cases, we normalize each  $x_{i,\ell,g}$  to range between 0 and 1. The problem is equivalent under linear  
456 transformations of  $x$ , but this normalization helps with computational performance. The intercept  
457 term, when used, is represented in  $x$  as a column of 1's.

## 458 Fitting the GLAMDE model

459 GLAMDE estimates the parameters of (1), (2), and (3) via maximum likelihood estimation. First, we  
 460 note that all parameters and parameter relationships in the model are independent across samples, so  
 461 we fit the model independently for each sample. We will return to the issue of population inference  
 462 across multiple samples in *Statistical inference on multiple samples/replicates*. Next, the parameters of  
 463  $\beta_{i,k}$  and  $\gamma_j$  are estimated by the RCTD algorithm as previously described [24]. We note that GLAMDE  
 464 can also optionally import cell type proportions from external cell type proportion identification meth-  
 465 ods [27, 28]. Here, some pixels are identified as single cell types while others as mixtures of multiple  
 466 cell types. We can accurately estimate cell type proportions and platform effects without being aware  
 467 of differential spatial gene expression because differential spatial gene expression is smaller than gene  
 468 expression differences across cell types. After determining cell type proportions, GLAMDE estimates  
 469 gene-specific overdispersion magnitude  $\sigma_{\varepsilon,j,g}$  for each gene by maximum likelihood estimation (see  
 470 *Supplementary Methods* for details). Finally, GLAMDE estimates the DE coefficients  $\alpha$  by maximum  
 471 likelihood estimation. For the final key step of estimating  $\alpha$ , we use plugin estimates (denoted by  $\hat{\cdot}$ )  
 472 of  $\beta$ ,  $\gamma$ , and  $\sigma_\varepsilon$ . After we substitute (3) into (1) and (2), we obtain:

$$Y_{i,j,g} \mid \varepsilon_{i,j,g} \sim \text{Poisson} \left\{ N_{i,g} \exp \left[ \log \left( \sum_{k=1}^K \hat{\beta}_{i,k,g} \exp \left( \alpha_{0,k,j,g} + \sum_{\ell=1}^L x_{i,\ell,g} \alpha_{\ell,k,j,g} \right) \right) + \hat{\gamma}_{j,g} + \varepsilon_{i,j,g} \right] \right\} \quad (4)$$

$$\varepsilon_{i,j,g} \sim \text{Normal}(0, \hat{\sigma}_{\varepsilon,j,g}^2), \quad (5)$$

473 We provide an algorithm for computing the maximum likelihood estimator of  $\alpha$ , presented in the  
 474 *Supplementary Methods*. Our likelihood optimization algorithm is a second-order, trust-region based  
 475 optimization (see *Supplementary Methods* for details). In brief, we iteratively solve quadratic approx-  
 476 imations of the log-likelihood, adaptively constraining the maximum parameter change at each step.  
 477 Critically, the likelihood is independent for each gene  $j$  (and sample  $g$ ), so separate genes are run in  
 478 parallel in which case there are  $K \times (L + 1)$   $\alpha$  parameters per gene and sample.

## 479 Hypothesis testing

480 In addition to estimating the vector  $\alpha_{j,g}$  (dimensions  $L + 1$  by  $K$ ) for gene  $j$  and sample  $g$ , we  
 481 can compute standard errors around  $\alpha_{j,g}$ . By asymptotic normality (see *Supplementary Methods* for  
 482 details), we have approximately that (setting  $n$  to be the total number of pixels),

$$\sqrt{n}(\hat{\alpha}_{j,g} - \alpha_{j,g}) \sim \text{Normal}(0, I_{\alpha_{j,g}}^{-1}), \quad (6)$$

483 where  $I_{\alpha_{j,g}}$  is the Fisher information of model (4), which is computed in the *Supplementary Methods*.  
 484 Given this result, we can compute standard errors, confidence intervals, and hypothesis tests. As a  
 485 consequence of (6), the standard error of  $\alpha_{\ell,k,j,g}$ , denoted  $s_{\ell,k,j,g}$ , is  $\sqrt{(I_{\alpha_{j,g}}^{-1})_{\ell,k}/n}$ .

486 First, we consider the case where we are interested in a single parameter,  $\alpha_{\ell,k,j,g}$ , for  $\ell$  and  $g$  fixed  
 487 and for each cell type  $k$  and gene  $j$ ; for example,  $\alpha_{\ell,k,j,g}$  could represent the log-fold-change between  
 488 two discrete regions. In this case, for each gene  $j$ , we compute the z-statistic,  $z_{\ell,k,j,g} = \frac{\alpha_{\ell,k,j,g}}{s_{\ell,k,j,g}}$ .  
 489 Using a two-tailed z-test, we compute a  $p$ -value for the null hypothesis that  $\alpha_{\ell,k,j,g} = 0$  as  $p_{\ell,k,j,g} =$   
 490  $2 * F(-|z_{\ell,k,j,g}|)$ , where  $F$  is the distribution function of the standard Normal distribution. Finally,  
 491  $q$ -values are calculated across all genes within a cell type in order to control the false discovery rate  
 492 using the Benjamini-Hochberg procedure [69]. We used a false discovery rate (FDR) of .01 (0.1 for  
 493 nonparametric case) and a fold-change cutoff of 1.5 (N/A for nonparametric case). Additionally, for  
 494 each cell type, genes were pre-filtered so that the expression within the cell type of interest had a total  
 495 expression of at least 15 unique molecular identifiers (UMIs) over all pixels and at least 50% as large  
 496 mean normalized expression as the expression within each other cell type.

497 For the multi-region case, we instead test for differences of pairs of parameters representing the  
498 average expression within each region. As a result,  $p$ -values are scaled up due to multiple hypothesis  
499 testing. We select genes which have significant differences between at least one pair of regions. For  
500 other cases in which we are interested in multiple parameters, for example the nonparametric case, we  
501 test each parameter individually and scale  $p$ -values due to multiple hypothesis testing.

## 502 Statistical inference on multiple samples/replicates

503 GLAMDE can be run on either one or multiple biological replicates and/or samples. In the case of  
504 multiple replicates, we recall  $\alpha_g$  and  $s_g$  are the differential expression and standard error for replicate  
505  $g$ , where  $1 \leq g \leq G$ , and  $G > 1$  is the total number of replicates. We now consider testing for  
506 differential expression across all replicates for covariate  $\ell$ , cell type  $k$ , and gene  $j$ . In this case, we  
507 assume that additional biological or technical variation across samples exists, such that each unknown  
508  $\alpha_g$  is normally distributed around a population-level differential expression  $A$ , with standard deviation  
509  $\tau$ :

$$\alpha_{\ell,k,j,g} \stackrel{i.i.d.}{\sim} \text{Normal}(A_{\ell,k,j}, \tau_{\ell,k,j}^2). \quad (7)$$

510 Under this assumption, and using (6) for the distribution of the observed single-sample estimates  $\hat{\alpha}$ ,  
511 we derive the following feasible generalized least squares estimator of  $A$  (see *Supplementary Methods*  
512 for details),

$$\hat{A}_{\ell,k,j} := \frac{\sum_{g=1}^G (\hat{\alpha}_{\ell,k,j,g}) / (\hat{\tau}_{\ell,k,j}^2 + s_{\ell,k,j,g}^2)}{\sum_{g=1}^G 1 / (\hat{\tau}_{\ell,k,j}^2 + s_{\ell,k,j,g}^2)}. \quad (8)$$

513 Here,  $\hat{\alpha}$  and  $s$  are obtained from GLAMDE estimates on individual samples (see (6)), whereas  $\hat{\tau}^2$   
514 represents the estimated variance across samples (Supplementary Figure 7). Please see the *Supple-*  
515 *mentary Methods* for additional details such as the method of moments procedure [70] for estimating  
516  $\hat{\tau}_{\ell,k,j}^2$  and the standard errors of  $A$ . Intuitively, our estimate of the population-level differential ex-  
517 pression is a variance-weighted sum over the DE estimates of individual replicates, and we note that  
518 our multiple-replicate approach is similar to widely used meta-analysis methods [70, 71]. As we have  
519 obtained estimates and standard errors of  $A$ , these are subsequently used in hypothesis testing for  
520 the hypothesis that  $A_{\ell,k,j} = 0$  in a manner identical to what is described above in *Hypothesis testing*  
521 for the single replicate case. We also derived a version of this estimator for the case where there are  
522 multiple biological samples and multiple replicates within each sample (*Supplementary Methods*).

## 523 Collection and preprocessing of scRNA-seq, spatial transcriptomics, amyloid 524 beta imaging, and HCR data

525 We collected four Alzheimer’s Slide-seq mouse hippocampus sections [38] using the Slide-seqV2 pro-  
526 tocol [2] (see *Supplementary Methods* for details) on a female 8.8 month old J20 Alzheimer’s mouse  
527 model [38]. We used three total Slide-seq mouse cerebellum sections, two collected using the Slide-  
528 seqV2 protocol, and one section used from a previous study [24]. Recall that data from multiple sections  
529 is integrated as described in *Multiple replicates*. The Slide-seq mouse testes and mouse cancer datasets  
530 were used from recent previous studies [12, 49]. In particular, the tumor dataset represented a single  
531  $Kras^{G12D/+} Trp53^{-/-}$  (KP) mouse metastatic lung adenocarcinoma tumor deposit in the liver [50]. The  
532 MERFISH hypothalamus dataset was obtained from a publicly available study [11]. To identify cell  
533 types on these datasets, we utilized publicly available single-cell RNA-seq datasets for the testes [72],  
534 hypothalamus [11], cerebellum [32], cancer [49], and Alzheimer’s hippocampus datasets [73]. All these  
535 scRNA-seq datasets have previously been annotated by cell type.

536 Slide-seq data was preprocessed using the Slide-seq tools pipeline [2]. For all spatial transcriptomics  
537 datasets, the region of interest (ROI) was cropped prior to running GLAMDE, and spatial transcrip-  
538 tomic spots were filtered to have a minimum of 100 UMIs. We used prior anatomical knowledge to

539 crop the ROI from an image of the total UMI counts per pixel across space, which in many cases allows  
540 one to observe overall anatomical features. For example, in Slide-seq Alzheimer’s hippocampus, the  
541 somatosensory cortex was cropped out prior to analysis.

542 For the Alzheimer’s dataset, in order to test for differential expression with respect to amyloid  
543 plaques, we collected fluorescent images of DAPI and amyloid beta ( $A\beta$ ), using IBL America Amyloid  
544 Beta (N) (82E1)  $A\beta$  Anti-Human Mouse IgG MoAb on sections adjacent to the Slide-seq data. We  
545 co-registered the DAPI image to the adjacent Slide-seq total UMI image using the `ManualAlignImages`  
546 function from the `STutility` R package [74]. To calculate plaque density, plaque images were convolved  
547 with an exponentially-decaying isotropic filter, using a threshold at the 0.9 quantile, and normalized  
548 to be between 0 and 1. For each Slide-seq section, plaque density was defined as the average between  
549 the plaque densities on the two adjacent amyloid sections.

550 For *in situ* RNA hybridization validation of cerebellum DE results, we collected hybridization chain  
551 reaction (HCR) data on genes *Aldoc*, *Kcnd2*, *Mybpc1*, *Plcb4*, and *Tmem132c* (Supplementary Table  
552 9) using a previously developed protocol [75]. We simultaneously collected cell type marker genes  
553 of Bergmann (*Gdf10*), granule (*Gabra6*), and Purkinje (*Calb1*) cell types, markers that were sourced  
554 from a prior cerebellum study [32]. Data from *Kcnd2* was removed due to the HCR fluorescent channel  
555 failing to localize RNA molecules, but rather reflecting tissue autofluorescence. ROIs of nodular and  
556 anterior regions were cropped, and background, defined as median signal, was subtracted. For this  
557 data, DE was calculated as the log-fold-change, across ROIs, of average gene signal over the pixels  
558 within the ROI containing cell type markers of a particular cell type. Pixels containing marker genes of  
559 multiple cell types were removed. GLAMDE single-sample standard errors in Figure 3d were calculated  
560 by modeling single-sample variance as the sum of the variance across samples and variance representing  
561 uncertainty around the population mean.

## 562 Cell type proportion estimation and construction of covariates

563 For each dataset, we constructed at least one covariate, an axis along which to test for DE. All  
564 covariates were scaled linearly to have minimum 0 and maximum 1. For the cerebellum dataset, the  
565 covariate was defined as an indicator variable representing membership within the nodular region (as  
566 opposed to the anterior region). The nodular and anterior ROIs were annotated manually from the  
567 total UMI image, and all other regions were removed. For the testes dataset, the covariate was a  
568 discrete variable representing the cellular microenvironment of tubule stage, labels that were obtained  
569 from tubule-level gene expression clustering from the previous Slide-seq testes study [12]. In that study  
570 and here, tubules are categorized into 4 main stages according to tubule sub-stage groups of stage I–III,  
571 IV–VI, VII–VIII, and IX–XII. For the cancer dataset, the covariate was chosen to be the density of the  
572 myeloid cell type. Cell type density was calculated by convolving the cell type locations, weighted by  
573 UMI number, with an exponential filter. For this dataset, we also ran GLAMDE nonparametrically.  
574 For the Alzheimer’s hippocampus dataset, the covariate was chosen to be the plaque density, defined  
575 in Section *Collection and preprocessing*. For the MERFISH hypothalamus dataset, the covariate was  
576 defined as distance to the midline, and we also considered quadratic functions of midline distance by  
577 adding squared distance as an covariate. For the quadratic MERFISH GLAMDE model, we conducted  
578 hypothesis testing on the quadratic coefficient. To estimate platform effects and cell type proportions,  
579 RCTD was run on *full mode* for the testes dataset, and was run on *doublet mode* for all other datasets  
580 with default parameters [24].

## 581 Validation with simulated gene expression dataset

582 We created a ground truth DE simulation to test GLAMDE on the challenging situation of mixtures  
583 between two cell type layers. We tested GLAMDE on a dataset of cell type mixtures simulated from  
584 the cerebellum single-nucleus RNA-seq dataset, which was also used as the reference for cell type  
585 mapping. We restricted to Purkinje and Bergmann cell types, which are known to spatially colocalize.  
586 In order to simulate a cell type mixture of cell types A (Purkinje) and B (Bergmann), we randomly

587 chose a cell from each cell type, and sampled a predefined number of UMIs from each cell (total  
588 1,000). We defined two discrete spatial regions (Figure 1a), populated with A/B cell type mixtures.  
589 We varied the mean cell type proportion difference across the two regions and also simulated the case  
590 of cell type proportions evenly distributed across the two regions. Cell type-specific spatial differential  
591 gene expression also was simulated across the two regions. To simulate cell type-specific differential  
592 expression in the gene expression step of the simulation, we multiplicatively scaled the expected gene  
593 counts within each cell of each cell type. An indicator variable for the two spatial bins was used as the  
594 GLAMDE covariate.

## 595 Additional computational analysis

596 For confidence intervals on data points or groups of data points (Figure 4d, Figure 4g), we used the  
597 predicted variance of data points from GLAMDE (see *Supplementary Methods* for details). Likewise,  
598 for such analysis we used predicted counts from GLAMDE at each pixel (*Supplementary Methods*).  
599 For the testes dataset, a cell type was considered to be present on a bead if the proportion of that  
600 cell type was at least 0.25 (Figure 4d). Additionally, cell type and stage-specific marker genes were  
601 defined as genes that had a fold-change of at least 1.5 within the cell type of interest compared to each  
602 other cell type. We also required significant cell type-specific differential expression between the stage  
603 of interest with all other stages (fold-change of at least 1.5, significance at the level of 0.001, Monte  
604 Carlo test on Z-scores). Cyclic genes were defined as genes whose minimum expression within a cell  
605 type occurred two tubule stages away from its maximum expression, up to log-space error of up to  
606 0.25.

607 For nonparametric GLAMDE on the tumor dataset, we used hierarchical Ward clustering to cluster  
608 quantile-normalized spatial gene expression patterns into 7 clusters. For gene set testing on the tumor  
609 dataset, we tested the 50 hallmark gene sets from the MSigDB database [76] for aggregate effects in  
610 GLAMDE differential expression estimates for the tumor cell type. For the nonparametric case, we  
611 used a binomial test with multiple hypothesis correction to test for enrichment of any of the 7 spatial  
612 clusters of GLAMDE-identified significant genes in any of the 50 gene sets. For the parametric case,  
613 we used a permutation test on the average value of GLAMDE  $Z$  scores for a gene set. That is, we  
614 modified an existing gene set enrichment procedure [77] by filtering for genes with a fold-change of  
615 at least 1.5 and using a two-sided permutation test rather than assuming normality. In both cases,  
616 we filtered to gene sets with at least 5 genes and we used Benjamini-Hochberg procedure across all  
617 gene sets to control the false discovery rate at 0.05. The proportion of variance not due to sampling  
618 noise (Figure 5b) was calculated by considering the difference between observed variance on normalized  
619 counts and the expected variance due to Poisson sampling noise.

620 We considered and tested several simple alternative methods to GLAMDE, which represent general  
621 classes of approaches. First, we considered a two-sample Z-test on single cells (defined as pixels with  
622 cell type proportion at least 0.9). Additionally, we tested *Bulk* differential expression, which estimated  
623 differential expression as the log-ratio of average normalized gene expression across two regions. The  
624 *Single* method of differential expression rounded cell type mixtures to the nearest single cell type and  
625 computed the log-ratio of gene expression of cells in that cell type. Finally, the *Decompose* method  
626 of differential expression used a previously-developed method to compute expected gene expression  
627 counts for each cell type [24], followed by computing the ratio of cell type-specific gene expression in  
628 each region.

## 629 Implementation details

630 GLAMDE is publicly available as part of the R package <https://github.com/dmcable/spacexr>. The  
631 quadratic program that arises in the GLAMDE optimization algorithm is solved using the *quadprog*  
632 package in R [78]. Prior to conducting analysis on GLAMDE output, all ribosomal proteins and  
633 mitochondrial genes were filtered out. Additional parameters used for running GLAMDE are shown in  
634 Supplementary Table 10. GLAMDE was tested on a Macintosh laptop computer with a 2.4 GHz Intel



635 Core i9 processor and 32GB of memory (we recommend at least 4GB of memory to run GLAMDE). For  
636 example, we timed GLAMDE with four cores on one of the Slide-seq cerebellum replicates, containing  
637 2,776 pixels across two regions, 5 cell types, and 4,812 genes. Under these conditions, GLAMDE  
638 ran in 13 minutes and 47 seconds (excluding the cell type assignment step in which computational  
639 efficiency has been described previously [24]).

## 640 Author Contributions

641 D.M.C., R.A.I., and F.C. conceived the study; F.C., E.M., E.Z.M., and D.C. designed the Slide-seq,  
642 antibody stain, and HCR experiments; E.M. generated the Slide-seq, antibody stain, and HCR data;  
643 D.M.C., R.A.I., and F.C. developed the statistical methods; D.M.C., F.C., and R.A.I. designed the  
644 analysis; D.M.C., S.Z., M.D., R.A.I., and F.C. analyzed the data; D.M.C., F.C., R.A.I., V.S., and H.C.  
645 interpreted biological results; V.S. annotated the tumor H&E stain; D.M.C., F.C., and R.A.I. wrote  
646 the manuscript; all authors read and approved the final manuscript.

## 647 Acknowledgements

648 We thank Luli Zou and Robert Stickels for providing valuable input on the analysis. We thank  
649 Tongtong Zhao and Zachary Chiang for generously providing the cancer Slide-seq data and providing  
650 helpful feedback. We thank Samuel Marsh for kindly providing mouse J20 Alzheimer's model samples.  
651 We thank members of the Chen lab, Irizarry lab, and Macosko lab including Tushar Kamath for helpful  
652 discussions and feedback. D.C. was supported by a Fannie and John Hertz Foundation Fellowship and  
653 an NSF Graduate Research Fellowship. This work was supported by an NIH Early Independence  
654 Award (DP5, 1DP5OD024583 to F.C.), the NHGRI (R01, R01HG010647 to F.C. and E.Z.M), as well  
655 as the Burroughs Wellcome Fund, the Searle Scholars Award, and the Merkin Institute to F.C.. R.A.I.  
656 was supported by NIH grants R35GM131802 and R01HG005220.

## 657 Conflict of Interest Statement

658 E.Z.M. and F.C. are listed as inventors on a patent application related to Slide-seq. F.C. is a paid  
659 consultant for Celsius Therapeutics and Atlas Bio.

## 660 Data Availability Statement

661 Slide-seq V2 data generated for this study is available at the Broad Institute Single Cell Portal [https://singlecell.broadinstitute.org/single\\_cell/study/SCP1663](https://singlecell.broadinstitute.org/single_cell/study/SCP1663). Additional publicly available data  
662 from other studies that was used for analysis is also included in this repository.  
663

## 664 Code Availability Statement

665 GLAMDE is implemented in the open-source R package *spacexr*, with source code freely available at  
666 <https://github.com/dmcable/spacexr>. Additional code used for analysis in this paper is available  
667 at <https://github.com/dmcable/spacexr/tree/master/AnalysisGLAMDE>.

## References

- 668
- 669 [1] Rodrigues, S. G. *et al.* Slide-seq: A scalable technology for measuring genome-wide expression at  
670 high spatial resolution. *Science* **363**, 1463–1467 (2019).
- 671 [2] Stickels, R. R. *et al.* Highly sensitive spatial transcriptomics at near-cellular resolution with  
672 Slide-seqV2. *Nature biotechnology* **39**, 313–319 (2021).
- 673 [3] Chen, K. H., Boettiger, A. N., Moffitt, J. R., Wang, S. & Zhuang, X. Spatially resolved, highly  
674 multiplexed RNA profiling in single cells. *Science* **348** (2015).
- 675 [4] Wang, X. *et al.* Three-dimensional intact-tissue sequencing of single-cell transcriptional states.  
676 *Science* **361** (2018).
- 677 [5] Eng, C. H. L. *et al.* Transcriptome-scale super-resolved imaging in tissues by RNA seqFISH+.  
678 *Nature* **568**, 235–239 (2019).
- 679 [6] Liu, Y. *et al.* High-spatial-resolution multi-omics sequencing via deterministic barcoding in tissue.  
680 *Cell* **183**, 1665–1681 (2020).
- 681 [7] 10x Genomics. 10x genomics: Visium spatial gene expression. [https://www.10xgenomics.com/  
682 solutions/spatial-gene-expression/](https://www.10xgenomics.com/solutions/spatial-gene-expression/) (2020).
- 683 [8] Zollinger, D. R., Lingle, S. E., Sorg, K., Beechem, J. M. & Merritt, C. R. GeoMx RNA assay: High  
684 multiplex, digital, spatial analysis of RNA in FFPE tissue. In *In Situ Hybridization Protocols*,  
685 331–345 (Springer, 2020).
- 686 [9] Alon, S. *et al.* Expansion sequencing: Spatially precise in situ transcriptomics in intact biological  
687 systems. *Science* **371** (2021).
- 688 [10] Maynard, K. R. *et al.* Transcriptome-scale spatial gene expression in the human dorsolateral  
689 prefrontal cortex. *Nature neuroscience* **24**, 425–436 (2021).
- 690 [11] Moffitt, J. R. *et al.* Molecular, spatial, and functional single-cell profiling of the hypothalamic  
691 preoptic region. *Science* **362** (2018).
- 692 [12] Chen, H. *et al.* Dissecting mammalian spermatogenesis using spatial transcriptomics. *Cell Reports*  
693 **37**, 109915 (2021).
- 694 [13] Chen, W.-T. *et al.* Spatial transcriptomics and in situ sequencing to study Alzheimer’s disease.  
695 *Cell* **182**, 976–991 (2020).
- 696 [14] Svensson, V., Teichmann, S. A. & Stegle, O. SpatialDE: identification of spatially variable genes.  
697 *Nature methods* **15**, 343–346 (2018).
- 698 [15] Edsgård, D., Johnsson, P. & Sandberg, R. Identification of spatial expression trends in single-cell  
699 gene expression data. *Nature methods* **15**, 339–342 (2018).
- 700 [16] Sun, S., Zhu, J. & Zhou, X. Statistical analysis of spatial expression patterns for spatially resolved  
701 transcriptomic studies. *Nature methods* **17**, 193–200 (2020).
- 702 [17] Zhu, J., Sun, S. & Zhou, X. SPARK-X: non-parametric modeling enables scalable and robust  
703 detection of spatial expression patterns for large spatial transcriptomic studies. *Genome Biology*  
704 **22**, 1–25 (2021).
- 705 [18] Dries, R. *et al.* Giotto: a toolbox for integrative analysis and visualization of spatial expression  
706 data. *Genome biology* **22**, 1–31 (2021).

- 707 [19] Butler, A., Hoffman, P., Smibert, P., Papalexi, E. & Satija, R. Integrating single-cell transcrip-  
708 tomic data across different conditions, technologies, and species. *Nature biotechnology* **36**, 411–420  
709 (2018).
- 710 [20] Love, M. I., Huber, W. & Anders, S. Moderated estimation of fold change and dispersion for  
711 RNA-seq data with DESeq2. *Genome biology* **15**, 1–21 (2014).
- 712 [21] Robinson, M. D., McCarthy, D. J. & Smyth, G. K. edgeR: a Bioconductor package for differential  
713 expression analysis of digital gene expression data. *Bioinformatics* **26**, 139–140 (2010).
- 714 [22] Smyth, G. K. Limma: linear models for microarray data. In *Bioinformatics and computational*  
715 *biology solutions using R and Bioconductor*, 397–420 (Springer, 2005).
- 716 [23] Haghverdi, L., Lun, A. T., Morgan, M. D. & Marioni, J. C. Batch effects in single-cell RNA-  
717 sequencing data are corrected by matching mutual nearest neighbors. *Nature biotechnology* **36**,  
718 421–427 (2018).
- 719 [24] Cable, D. M. *et al.* Robust decomposition of cell type mixtures in spatial transcriptomics. *Nature*  
720 *Biotechnology* 1–10 (2021).
- 721 [25] Regev, A. *et al.* Science forum: the human cell atlas. *Elife* **6**, e27041 (2017).
- 722 [26] Petukhov, V. *et al.* Cell segmentation in imaging-based spatial transcriptomics. *Nature Biotech-*  
723 *nology* 1–10 (2021).
- 724 [27] Andersson, A. *et al.* Single-cell and spatial transcriptomics enables probabilistic inference of cell  
725 type topography. *Communications biology* **3**, 1–8 (2020).
- 726 [28] Dong, R. & Yuan, G. C. SpatialDWLS: accurate deconvolution of spatial transcriptomic data.  
727 *Genome biology* **22**, 1–10 (2021).
- 728 [29] Zhao, E. *et al.* Spatial transcriptomics at subspot resolution with BayesSpace. *Nature Biotech-*  
729 *nology* 1–10 (2021).
- 730 [30] Hardin, J. W., Hardin, J. W., Hilbe, J. M. & Hilbe, J. *Generalized linear models and extensions*  
731 (Stata press, 2007).
- 732 [31] Wood, S. & Wood, M. S. Package 'mgcv'. *R package version* **1**, 29 (2015).
- 733 [32] Kozareva, V. *et al.* A transcriptomic atlas of mouse cerebellar cortex comprehensively defines cell  
734 types. *Nature* **598**, 214–219 (2021).
- 735 [33] Zhao, M., Shirley, C. R., Mounsey, S. & Meistrich, M. L. Nucleoprotein transitions during  
736 spermiogenesis in mice with transition nuclear protein Tnp1 and Tnp2 mutations. *Biology of*  
737 *reproduction* **71**, 1016–1025 (2004).
- 738 [34] Hasegawa, K. & Saga, Y. Retinoic acid signaling in Sertoli cells regulates organization of the  
739 blood-testis barrier through cyclical changes in gene expression. *Development* **139**, 4347–4355  
740 (2012).
- 741 [35] Xu, J. *et al.* Computerized spermatogenesis staging (CSS) of mouse testis sections via quantitative  
742 histomorphological analysis. *Medical image analysis* **70**, 101835 (2021).
- 743 [36] Zhou, X. *et al.* Cellular and molecular properties of neural progenitors in the developing mam-  
744 malian hypothalamus. *Nature communications* **11**, 1–16 (2020).
- 745 [37] Romanov, R. A. *et al.* Molecular interrogation of hypothalamic organization reveals distinct  
746 dopamine neuronal subtypes. *Nature neuroscience* **20**, 176–188 (2017).

- 747 [38] Mucke, L. *et al.* High-level neuronal expression of A $\beta$ 1–42 in wild-type human amyloid protein  
748 precursor transgenic mice: Synaptotoxicity without plaque formation. *Journal of Neuroscience*  
749 **20**, 4050–4058 (2000). URL <https://www.jneurosci.org/content/20/11/4050>. <https://www.jneurosci.org/content/20/11/4050.full.pdf>.  
750
- 751 [39] Kraft, A. W. *et al.* Attenuating astrocyte activation accelerates plaque pathogenesis in APP/PS1  
752 mice. *The FASEB Journal* **27**, 187–198 (2013).
- 753 [40] Hong, S. *et al.* Complement and microglia mediate early synapse loss in Alzheimer mouse models.  
754 *Science* **352**, 712–716 (2016).
- 755 [41] Zhou, Y. *et al.* Human and mouse single-nucleus transcriptomics reveal TREM2-dependent and  
756 TREM2-independent cellular responses in Alzheimer’s disease. *Nature medicine* **26**, 131–142  
757 (2020).
- 758 [42] Veerhuis, R. *et al.* Cytokines associated with amyloid plaques in Alzheimer’s disease brain stim-  
759 ulate human glial and neuronal cell cultures to secrete early complement proteins, but not C1-  
760 inhibitor. *Experimental neurology* **160**, 289–299 (1999).
- 761 [43] Bernstein, H. G. & Keilhoff, G. Putative roles of cathepsin B in Alzheimer’s disease pathology:  
762 The good, the bad, and the ugly in one? *Neural regeneration research* **13**, 2100 (2018).
- 763 [44] Sobue, A. *et al.* Microglial gene signature reveals loss of homeostatic microglia associated with  
764 neurodegeneration of Alzheimer’s disease. *Acta neuropathologica communications* **9**, 1–17 (2021).
- 765 [45] DePaula-Silva, A. B. *et al.* Differential transcriptional profiles identify microglial-and macrophage-  
766 specific gene markers expressed during virus-induced neuroinflammation. *Journal of neuroinflam-*  
767 *mation* **16**, 1–20 (2019).
- 768 [46] Keren-Shaul, H. *et al.* A unique microglia type associated with restricting development of  
769 alzheimer’s disease. *Cell* **169**, 1276–1290 (2017).
- 770 [47] Serrano-Pozo, A., Das, S. & Hyman, B. T. APOE and Alzheimer’s disease: advances in genetics,  
771 pathophysiology, and therapeutic approaches. *The Lancet Neurology* **20**, 68–80 (2021).
- 772 [48] Mendsaikhan, A., Tooyama, I. & Walker, D. G. Microglial progranulin: involvement in Alzheimer’s  
773 disease and neurodegenerative diseases. *Cells* **8**, 230 (2019).
- 774 [49] Zhao, T. *et al.* Spatial genomics enables multi-modal study of clonal heterogeneity in tissues.  
775 *Nature* 1–7 (2021).
- 776 [50] Johnson, L. *et al.* Somatic activation of the K-ras oncogene causes early onset lung cancer in  
777 mice. *Nature* **410**, 1111–1116 (2001).
- 778 [51] Dang, C. V. c-Myc target genes involved in cell growth, apoptosis, and metabolism. *Molecular*  
779 *and cellular biology* **19**, 1–11 (1999).
- 780 [52] Jiménez-Sánchez, J. *et al.* Evolutionary dynamics at the tumor edge reveal metabolic imaging  
781 biomarkers. *Proceedings of the National Academy of Sciences* **118** (2021).
- 782 [53] Kodama, M. *et al.* In vivo loss-of-function screens identify KPNB1 as a new druggable oncogene  
783 in epithelial ovarian cancer. *Proceedings of the National Academy of Sciences* **114**, E7301–E7310  
784 (2017).
- 785 [54] Du, W. *et al.* KPNB1-mediated nuclear translocation of PD-L1 promotes non-small cell lung  
786 cancer cell proliferation via the Gas6/MerTK signaling pathway. *Cell Death & Differentiation*  
787 **28**, 1284–1300 (2021).

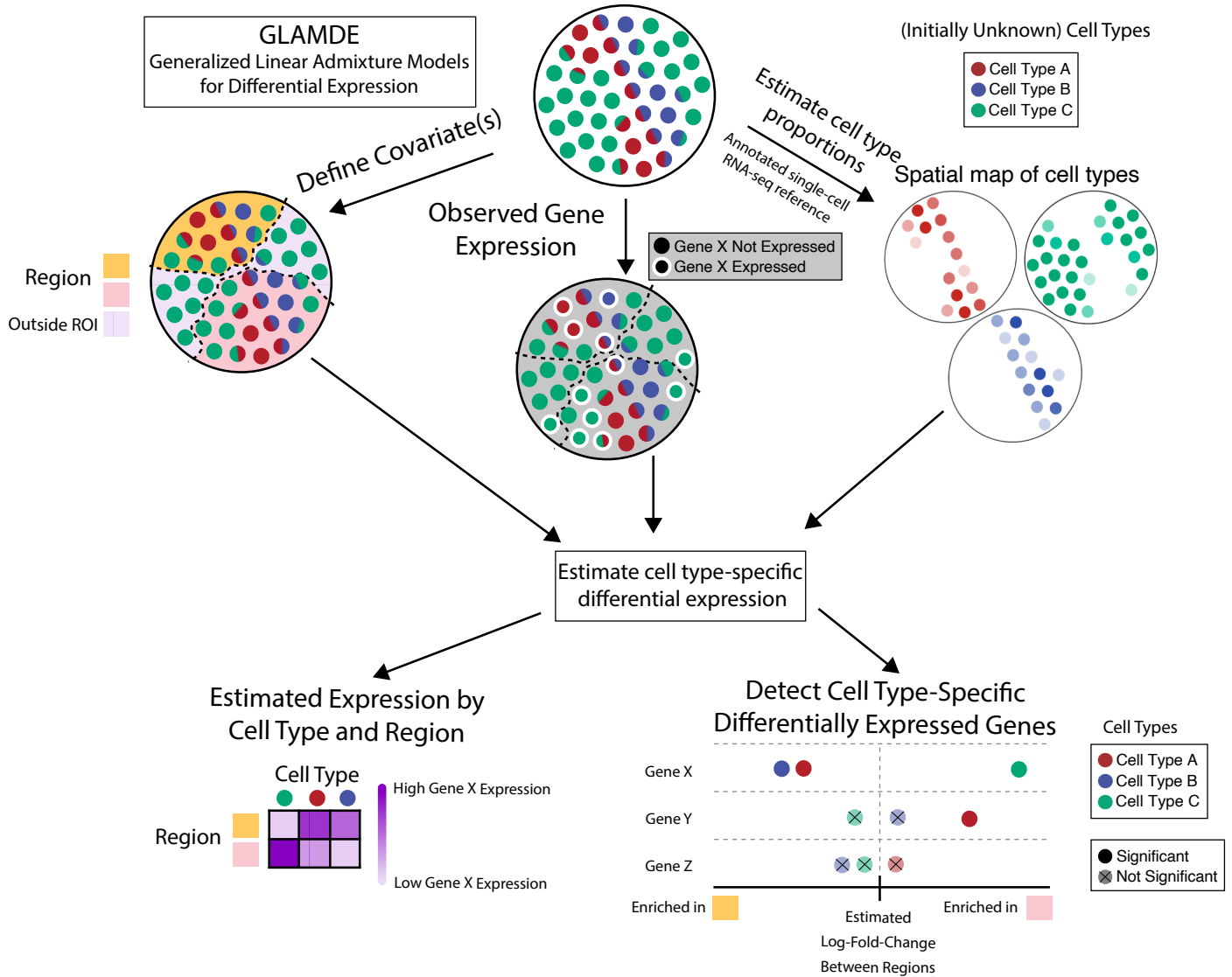
- 788 [55] Chen, D. P. *et al.* Peritumoral monocytes induce cancer cell autophagy to facilitate the progression  
789 of human hepatocellular carcinoma. *Autophagy* **14**, 1335–1346 (2018).
- 790 [56] Casanova-Acebes, M. *et al.* Tissue-resident macrophages provide a pro-tumorigenic niche to early  
791 nsclc cells. *Nature* 1–7 (2021).
- 792 [57] Che, D. *et al.* Macrophages induce EMT to promote invasion of lung cancer cells through the  
793 IL-6-mediated COX-2/PGE2/ $\beta$ -catenin signalling pathway. *Molecular immunology* **90**, 197–210  
794 (2017).
- 795 [58] Gschwandtner, M., Derler, R. & Midwood, K. S. More than just attractive: how CCL2 influences  
796 myeloid cell behavior beyond chemotaxis. *Frontiers in immunology* **10**, 2759 (2019).
- 797 [59] Lim, S. Y., Yuzhalin, A. E., Gordon-Weeks, A. N. & Muschel, R. J. Targeting the CCL2-CCR2  
798 signaling axis in cancer metastasis. *Oncotarget* **7**, 28697 (2016).
- 799 [60] Pires, B. R. *et al.* NF-kappaB is involved in the regulation of EMT genes in breast cancer cells.  
800 *PloS one* **12**, e0169622 (2017).
- 801 [61] Huber, M. A. *et al.* NF- $\kappa$ B is essential for epithelial-mesenchymal transition and metastasis in a  
802 model of breast cancer progression. *The Journal of clinical investigation* **114**, 569–581 (2004).
- 803 [62] Dongre, A. & Weinberg, R. A. New insights into the mechanisms of epithelial-mesenchymal  
804 transition and implications for cancer. *Nature reviews Molecular cell biology* **20**, 69–84 (2019).
- 805 [63] Wightman, D. P. *et al.* A genome-wide association study with 1,126,563 individuals identifies new  
806 risk loci for Alzheimer’s disease. *Nature genetics* **53**, 1276–1282 (2021).
- 807 [64] Satoh, J.-i. *et al.* TMEM106B expression is reduced in Alzheimer’s disease brains. *Alzheimer’s*  
808 *research & therapy* **6**, 1–14 (2014).
- 809 [65] Walker, D. G., Kim, S. U. & McGeer, P. L. Expression of complement C4 and C9 genes by human  
810 astrocytes. *Brain research* **809**, 31–38 (1998).
- 811 [66] Götzl, J. K. *et al.* Opposite microglial activation stages upon loss of PGRN or TREM 2 result in  
812 reduced cerebral glucose metabolism. *EMBO molecular medicine* **11**, e9711 (2019).
- 813 [67] Minami, S. S. *et al.* Progranulin protects against amyloid  $\beta$  deposition and toxicity in alzheimer’s  
814 disease mouse models. *Nature medicine* **20**, 1157–1164 (2014).
- 815 [68] Zhang, J. *et al.* Neurotoxic microglia promote TDP-43 proteinopathy in progranulin deficiency.  
816 *Nature* **588**, 459–465 (2020).
- 817 [69] Benjamini, Y. & Hochberg, Y. Controlling the false discovery rate: a practical and powerful  
818 approach to multiple testing. *Journal of the Royal statistical society: series B (Methodological)*  
819 **57**, 289–300 (1995).
- 820 [70] DerSimonian, R. & Laird, N. Meta-analysis in clinical trials. *Controlled clinical trials* **7**, 177–188  
821 (1986).
- 822 [71] Veroniki, A. A. *et al.* Methods to estimate the between-study variance and its uncertainty in  
823 meta-analysis. *Research synthesis methods* **7**, 55–79 (2016).
- 824 [72] Green, C. D. *et al.* A comprehensive roadmap of murine spermatogenesis defined by single-cell  
825 RNA-seq. *Developmental cell* **46**, 651–667 (2018).
- 826 [73] Saunders, A. *et al.* Molecular diversity and specializations among the cells of the adult mouse  
827 brain. *Cell* **174**, 1015–1030 (2018).



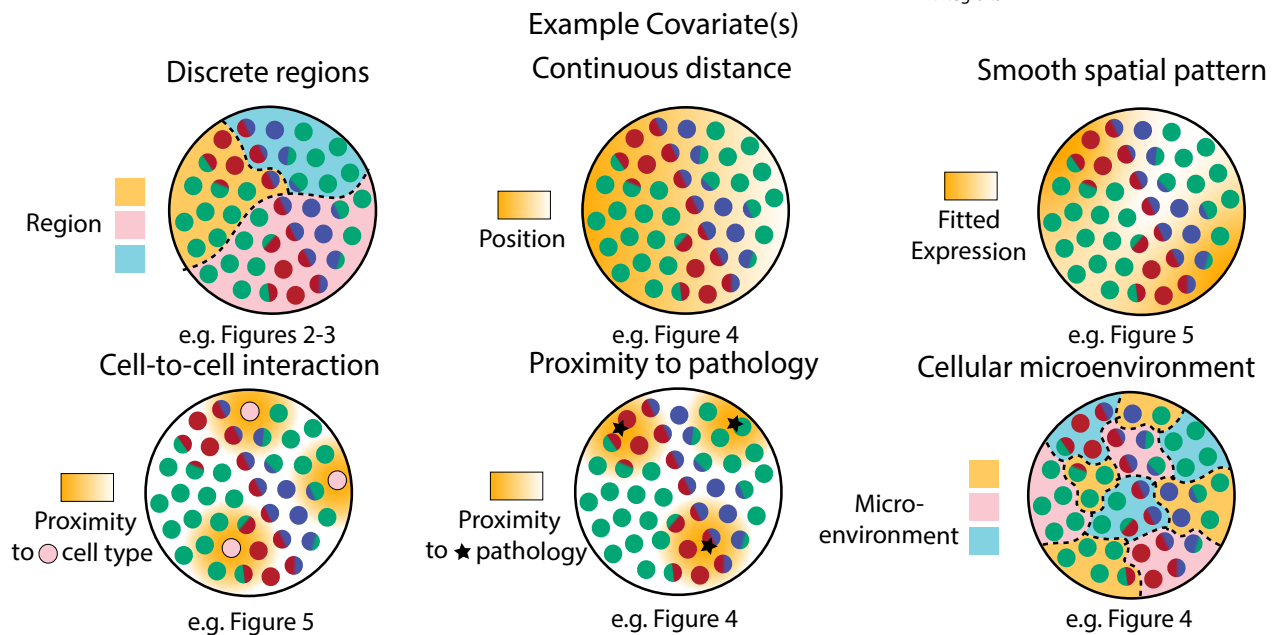
- 828 [74] Bergenstråhle, J., Larsson, L. & Lundeberg, J. Seamless integration of image and molecular  
829 analysis for spatial transcriptomics workflows. *BMC genomics* **21**, 1–7 (2020).
- 830 [75] Dirks, R. M. & Pierce, N. A. Triggered amplification by hybridization chain reaction. *Proceedings*  
831 *of the National Academy of Sciences* **101**, 15275–15278 (2004).
- 832 [76] Liberzon, A. *et al.* Molecular signatures database (MSigDB) 3.0. *Bioinformatics* **27**, 1739–1740  
833 (2011).
- 834 [77] Irizarry, R. A., Wang, C., Zhou, Y. & Speed, T. P. Gene set enrichment analysis made simple.  
835 *Statistical methods in medical research* **18**, 565–575 (2009).
- 836 [78] Turlach, B. A. & Weingessel, A. quadprog: Functions to solve quadratic programming problems.  
837 R package version 1.5-5 (2013).
- 838 [79] Yuan, Y. X. A review of trust region algorithms for optimization. In *Iciam*, vol. 99, 271–282  
839 (2000).
- 840 [80] Van der Vaart, A. W. *Asymptotic statistics*, vol. 3 (Cambridge university press, 2000).

841 **Figures**

a)



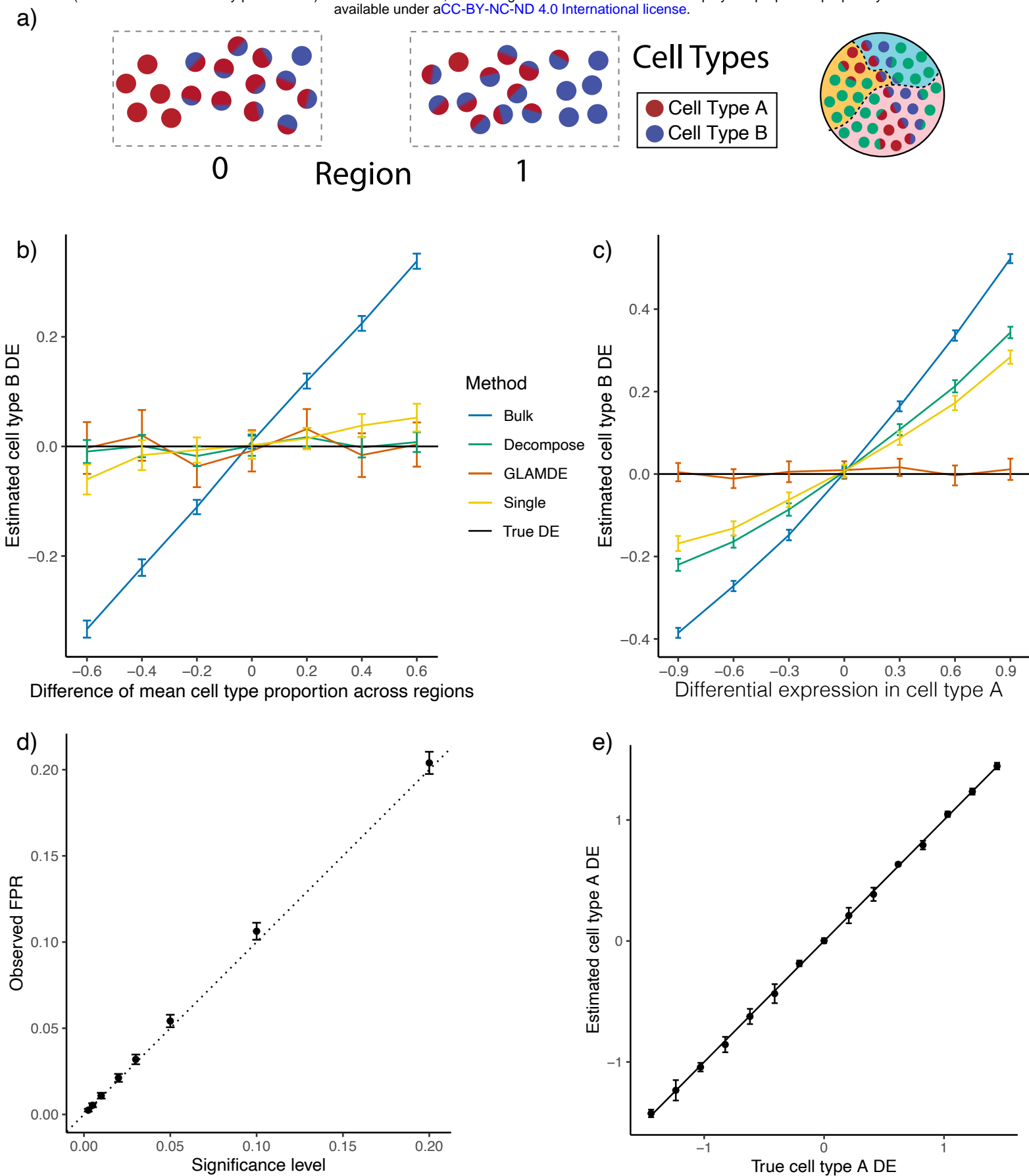
b)



842 Figure 1: Generalized Linear Admixture Models for Differential Expression learns cell type-specific  
843 differential expression from spatial transcriptomics data.

844 (a) Schematic of the GLAMDE Method. Top: GLAMDE inputs: a spatial transcriptomics dataset  
845 with observed gene expression (potentially containing cell type mixtures) and a covariate for differ-  
846 ential expression. Middle: GLAMDE first assigns cell types to the spatial transcriptomics dataset,  
847 and covariates are defined. Bottom: GLAMDE estimates cell type-specific gene expression along  
848 the covariate axes.

849 (b) Example covariates for explaining differential expression with GLAMDE. Top: Segmentation into  
850 multiple regions, continuous distance from some feature, or general smooth patterns (nonparamet-  
851 ric). Bottom: density of interaction with another cell type or pathological feature or a discrete  
852 covariate representing the cellular microenvironment.





853 Figure 2: GLAMDE provides unbiased estimates of cell type-specific differential expression in  
854 simulated data.

855 All: GLAMDE was tested on a dataset of simulated mixtures of single cells from a single-nucleus  
856 RNA-seq cerebellum dataset. Differential expression (DE) axes represent DE in log<sub>2</sub>-space of region 1  
857 w.r.t. region 0.

858 (a) Pixels are grouped into two regions, and genes are simulated with ground truth DE across regions.  
859 Each region contains pixels containing mixtures of various proportions between cell type A and  
860 cell type B. The difference in average cell type proportion across regions is varied across simulation  
861 conditions.

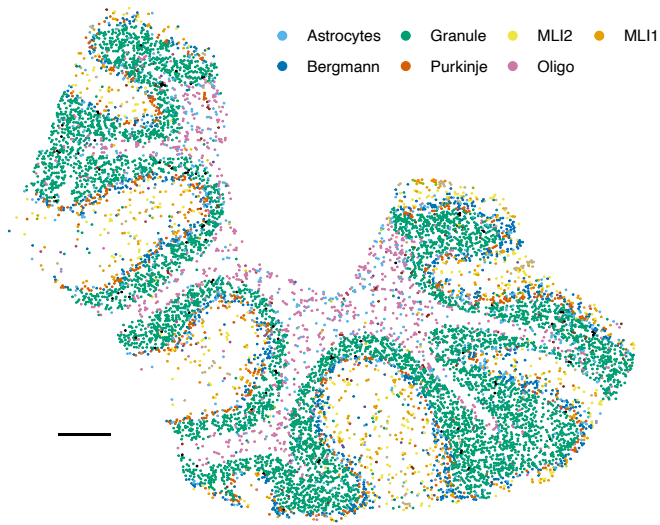
862 (b) Mean estimated cell type B *Astn2* DE (differential expression) across two regions as a function of  
863 the difference in mean cell type proportion across regions. *Astn2* is simulated with ground truth 0  
864 spatial DE, and an average of ( $n = 100$ ) estimates is shown, along with standard errors. Black line  
865 represents ground truth 0 DE (cell type B). Four methods are shown: *Bulk*, *Decompose*, *Single*,  
866 and *GLAMDE* (see *Methods* for details).

867 (c) Same as (b) for *Nrxn3* cell type B differential gene expression as a function of DE in cell type A,  
868 where *Nrxn3* is simulated to have DE within cell type A but no DE in cell type B.

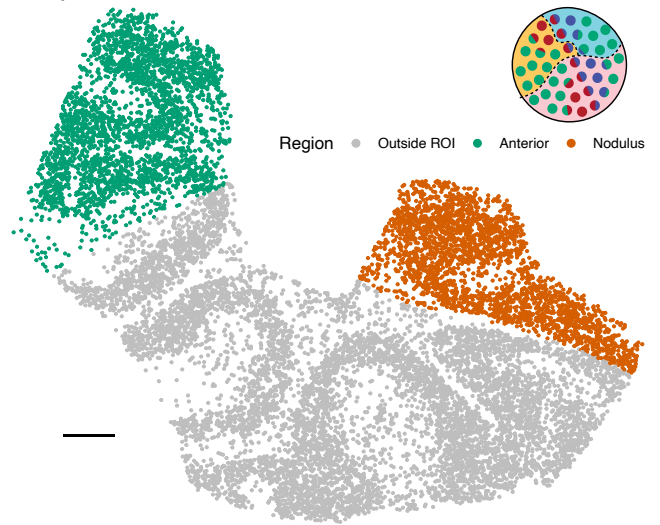
869 (d) For each significance level, GLAMDE's false positive rate (FPR), along with ground truth identity  
870 line (s.e. shown,  $n = 1500$ , 15 genes, 100 replicates per gene).

871 (e) GLAMDE mean estimated cell type A differential expression vs. true cell type A differential  
872 expression (average over  $n = 500$  replicates, s.e. shown). Ground truth identity line is shown, and  
873 one gene is used for the simulation per DE condition (out of 15 total genes).

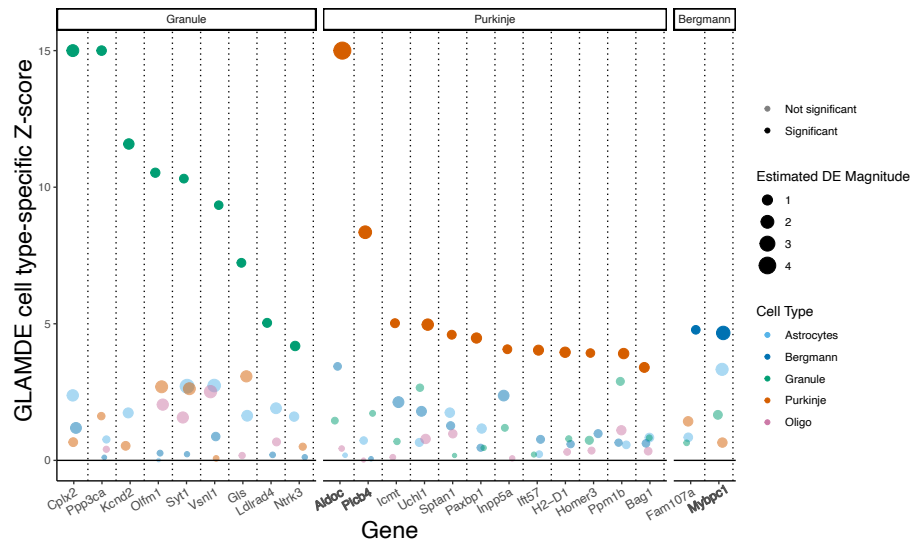
a)



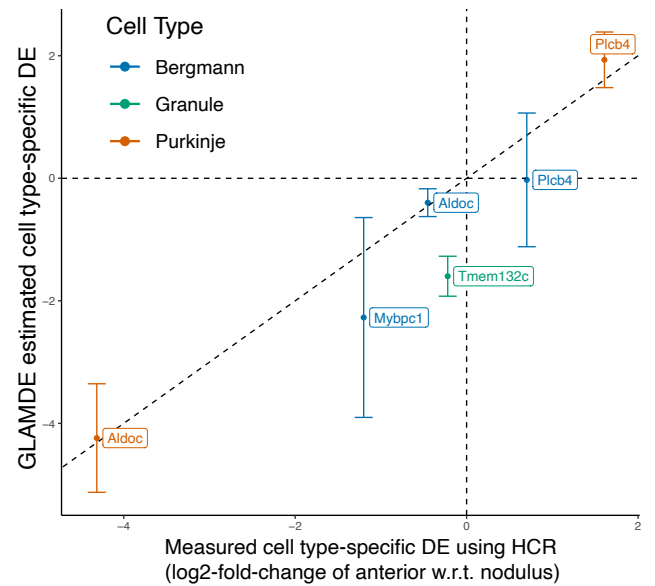
b)



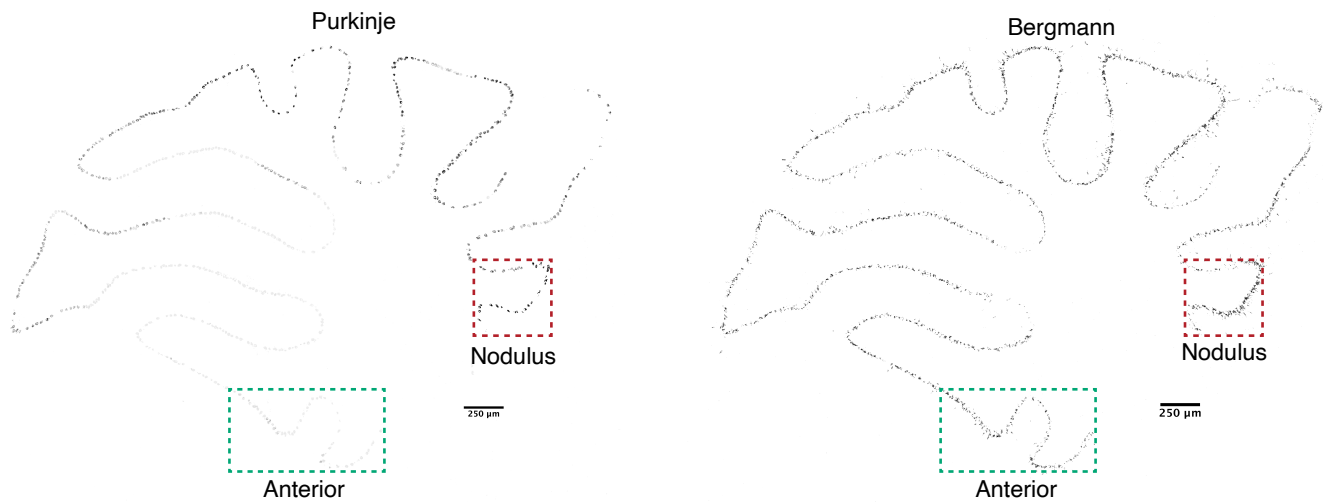
c)



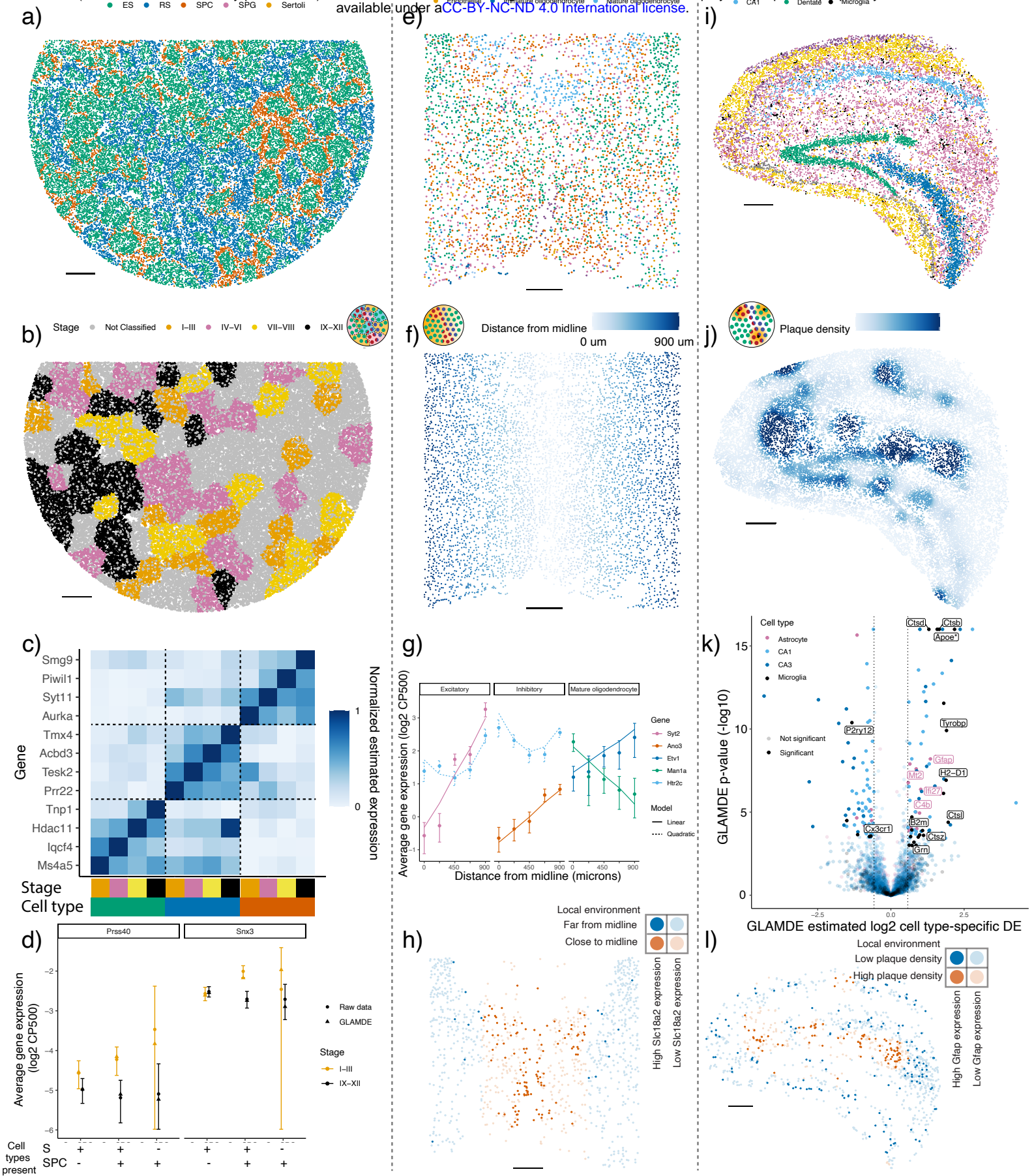
d)



e)



- 874 Figure 3: GLAMDE's estimated cell type-specific differential expression is validated by HCR-FISH.
- 875 (a) GLAMDE's spatial map of cell type assignments in the cerebellum Slide-seq dataset. Out of 19 cell  
876 types, the seven most common appear in the legend. Reproduced from [24]. Three total replicates  
877 were used to fit GLAMDE.
- 878 (b) Covariate used for GLAMDE, representing the anterior lobule region (green) and nodulus (red).  
879 Schematic refers to the GLAMDE problem type outlined in Figure 1b.
- 880 (c) GLAMDE Z-score for testing for DE for each gene and for each cell type. Genes are grouped by  
881 cell type with maximum estimated DE, and estimated DE magnitude appears as size of the points.  
882 Bold genes appear below in HCR validation.
- 883 (d) Scatterplot of GLAMDE DE estimates vs. HCR measurements for cell type-specific log<sub>2</sub> differential  
884 expression. Positive values indicate gene expression enrichment in the anterior region. Error bars  
885 represent GLAMDE confidence intervals for predicted DE on a new biological replicate. A dotted  
886 identity line is shown, and cell types are colored.
- 887 (e) HCR images of *Aldoc* continuous gene expression. Only pixels with high cell type marker measure-  
888 ments for Purkinje (left) and Bergmann (right) are shown. Regions of interest (ROIs) of nodulus  
889 and anterior regions are outlined in green and red, respectively.
- 890 All scale bars 250 microns.





891 Figure 4: GLAMDE discovers cell type-specific differential expression in a diverse set of problems  
892 on testes, Alzheimer’s hippocampus, and hypothalamus datasets.

893 All panels: results of GLAMDE on the Slide-seqV2 testes (left column), MERFISH hypothal-  
894 amus (middle column), and Slide-seqV2 Alzheimer’s hippocampus (right column). Schematics in b,f,j  
895 reference GLAMDE problem types (Figure 1b).

896 (a) GLAMDE’s spatial map of cell type assignments in testes. All cell types are shown, and the most  
897 common cell types appear in the legend.

898 (b) Covariate used for GLAMDE in testes: four discrete tubule stages.

899 (c) Cell type and tubule stage-specific genes identified by GLAMDE. GLAMDE estimated expression  
900 is standardized between 0 and 1 for each gene. Columns represent GLAMDE estimates for each  
901 cell type and tubule stage.

902 (d) Log2 average expression (in counts per 500 (CP500)) of pixels grouped based on tubule stage and  
903 presence or absence of spermatid (S) cell types (defined as elongating spermatid (ES) or round  
904 spermatid (RS)) and/or spermatocyte (SPC) cell type. Circles represent raw data averages while  
905 triangles represent GLAMDE predictions, and error bars around circular points represent  $\pm 1.96$   
906 s.d. (*Supplementary methods*). Genes *Prss40* and *Snx3* are shown on left and right, respectively.

907 (e) Same as (a) for hypothalamus.

908 (f) Covariate used for GLAMDE in hypothalamus: continuous distance from midline.

909 (g) Log2 average expression (in counts per 500 (CP500)) of genes identified to be significantly differ-  
910 entially expressed by GLAMDE for each of the excitatory, inhibitory, and mature oligodendrocyte  
911 cell types. Single cell type pixels are binned according to distance from midline, and points repre-  
912 sent raw data averages while lines represents GLAMDE predictions and error bars around points  
913 represent  $\pm 1.96$  s.d. (*Supplementary methods*).

914 (h) Spatial visualization of *Slc18a2*, whose expression within inhibitory neurons was identified by  
915 GLAMDE to depend on midline distance. Red/blue represents inhibitory neurons close/far to  
916 midline, respectively. Bold points inhibitory neurons expressing *Slc18a2* at a level of at least 10  
917 counts per 500.

918 (i) Same as (a) for Alzheimer’s hippocampus, where four total replicates were used to fit GLAMDE.

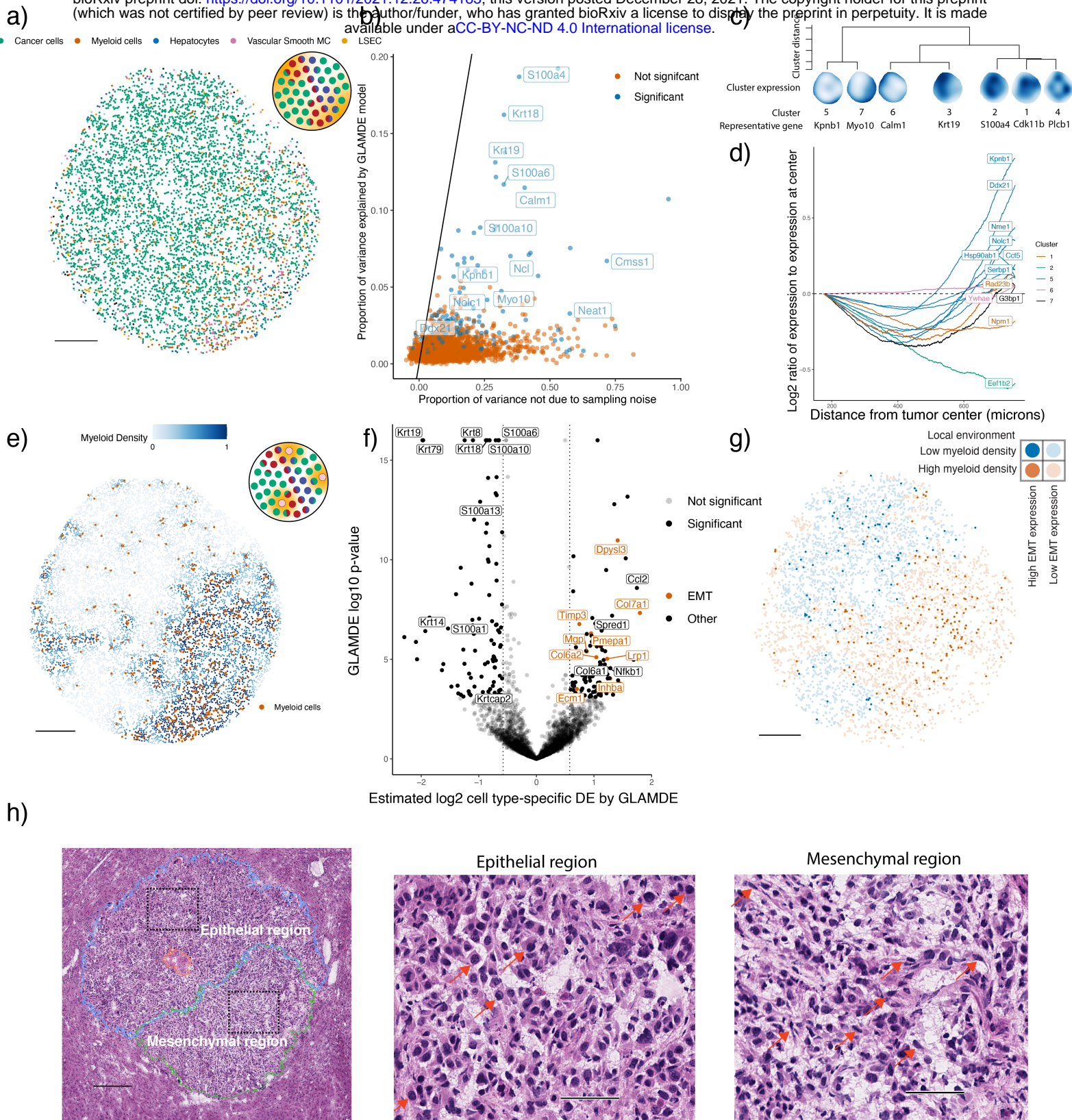
919 (j) Covariate used for GLAMDE in Alzheimer’s hippocampus: continuous density of beta-amyloid  
920 ( $A\beta$ ) plaque.

921 (k) Volcano plot of GLAMDE differential expression results in log2-space, with positive values cor-  
922 responding to plaque-upregulated genes. Color represents cell type, and a subset of significant  
923 genes are labeled. Dotted lines represents 1.5x fold-change cutoff used for GLAMDE. (\*): *ApoE*  
924 didn’t pass default GLAMDE gene filters(*Methods*) because 4x higher expression in astrocytes  
925 than microglia.

926 (l) Spatial visualization of *Gfap*, whose expression within astrocytes was identified by GLAMDE to  
927 depend on plaque density. Red/blue represents the astrocytes in high/low plaque density areas,  
928 respectively. Bold points represent astrocytes expressing *Gfap* at a level of at least 1 count per  
929 500.

930 All scale bars 250 microns.





931 Figure 5: GLAMDE enables the discovery of differentially expressed pathways in a *Kras*<sup>G12D/+</sup>  
932 *Trp53*<sup>-/-</sup> (KP) mouse model.

933 All panels: GLAMDE was run on multiple cell types, but plots represent GLAMDE results on the  
934 tumor cell type. Nonparametric GLAMDE results are shown in panels b–d, while parametric GLAMDE  
935 results are shown in panels e–h.

936 (a) GLAMDE’s spatial map of cell type assignments. Out of 14 cell types, the five most common  
937 appear in the legend.

938 (b) Scatter plot of GLAMDE  $R^2$  and overdispersion (defined as proportion of variance not due to  
939 sampling noise) for nonparametric GLAMDE results on the tumor cell type. Identity line is  
940 shown, representing the maximum possible variance that could be explained by any model.

941 (c) Dendrogram of hierarchical clustering of ( $n = 162$  significant genes) GLAMDE’s fitted smooth  
942 spatial patterns at the resolution of 7 clusters. Each spatial plot represents the average fitted gene  
943 expression patterns over the genes in each cluster.

944 (d) Moving average plot of GLAMDE fitted gene expression (normalized to expression at center) as a  
945 function of distance from the center of the tumor for 12 genes in the *Myc* targets pathway identified  
946 to be significantly spatially differentially expressed by GLAMDE.

947 (e) Covariate used for parametric GLAMDE: continuous density of myeloid cell types in the tumor.  
948 Schematic refers to GLAMDE problem type (Figure 1b).

949 (f) Volcano plot of GLAMDE log<sub>2</sub> differential expression results on the tumor cell type with positive  
950 values representing upregulation in the presence of myeloid immune cells. A subset of significant  
951 genes are labeled, and dotted lines represent 1.5x fold-change cutoff.

952 (g) Spatial plot of total expression in tumor cells of the 9 differentially expressed epithelial-mesenchymal  
953 transition (EMT) genes identified by GLAMDE in (f). Red represents the tumor cells in high  
954 myeloid density areas, whereas blue represents tumor cells in regions of low myeloid density. Bold  
955 points represent tumor cells expressing these EMT genes at a level of at least 2.5 counts per 500.

956 (h) Hematoxylin and eosin (H&E) image of adjacent section of the tumor. Left: mesenchymal (green),  
957 necrosis (red), and epithelial (blue) annotated tumor regions, with dotted boxes representing ep-  
958 ithelial and mesenchymal areas of focus for the other two panels. Middle/right: enlarged images  
959 of epithelial (middle) or mesenchymal (right) regions. Red arrows point to example tumor cells  
960 with epithelial (middle) or mesenchymal (right) morphology.

961 All scale bars 250 microns, except for (h) middle/right, which has 50 micron scale bars.

## 962 Supplementary Methods

### 963 Introduction and model definition

964 We now revisit our Generalized Linear Admixture Models for Differential Expression (GLAMDE)  
965 model at an increased level of detail. Recall the following definition of the GLAMDE model, where for  
966 each pixel  $i = 1, \dots, I$  in the spatial transcriptomics dataset, we denote the observed gene expression  
967 counts as  $Y_{i,j,g}$  for each gene  $j = 1, \dots, J$  and experimental sample  $g = 1, \dots, G$ :

$$Y_{i,j,g} \mid \lambda_{i,j,g} \sim \text{Poisson}(N_{i,g}\lambda_{i,j,g}) \quad (9)$$
$$\log(\lambda_{i,j,g}) = \log\left(\sum_{k=1}^K \beta_{i,k,g}\mu_{i,k,j,g}\right) + \gamma_{j,g} + \varepsilon_{i,j,g},$$

968 with  $N_{i,g}$  the total transcript count or number of unique molecular identifies (UMIs) for pixel  $i$  and  
969 sample  $g$ ,  $K$  the number of cell types present in our dataset,  $\mu_{k,j,g}$  the mean gene expression profile for  
970 cell type  $k$  and gene  $j$  and sample  $g$ ,  $\beta_{i,k,g}$  the proportion of the contribution of cell type  $k$  to pixel  $i$   
971 in sample  $g$ ,  $\gamma_{j,g}$  a gene-specific platform random effect, and  $\varepsilon_{i,j,g}$  a random effect to account for other  
972 technical and biological sources of variation. We assume  $\gamma_{j,g}$  and  $\varepsilon_{i,j,g}$  both follow normal distributions  
973 with mean 0 and standard deviation  $\sigma_{\gamma,g}$  and  $\sigma_{\varepsilon,j,g}$ , respectively. Lastly,  $\mu_{i,k,j,g}$  represents the average  
974 gene expression of gene  $j$  in cell type  $k$  at pixel location  $i$  in sample  $g$ . We model  $\mu_{i,k,j,g}$ , for each gene  
975  $j$ , each cell type  $k$ , and each sample  $g$  as depending log-linearly on several covariates,  $x$ :

$$\log(\mu_{i,k,j,g}) = \alpha_{2,0,k,j,g} + \sum_{\ell=1}^{L_1} x_{1,i,\ell,g}\alpha_{1,\ell,j,g} + \sum_{\ell=1}^{L_2} x_{2,i,\ell,g}\alpha_{2,\ell,k,j,g}. \quad (10)$$

976 More specifically, we split our covariates into two sets (of sizes  $L_1$  and  $L_2$ ). The first set,  $x_{1,i,\ell,g}$ , share  
977 coefficients across cell types, while the second set,  $x_{2,i,\ell,g}$ , has a different coefficient for each cell type.  
978 This notation is different from the presentation of GLAMDE in the main methods section, in which  
979  $x_1$  was not present and no coefficients were shared across cell types. In practice, we do not typically  
980 assume that differential expression is shared across cell types (that is,  $x_{1,i,\ell,g}$  is not used), but  $x_1$  is  
981 included here as an optional feature. We have  $x_{\cdot,i,\ell,g}$  representing the  $\ell$ 'th covariate, evaluated at  
982 pixel  $i$  in sample  $g$ . In all cases,  $x$  is pre-determined to contain variables on which gene expression is  
983 hypothesized to depend.

984 For each covariate  $x$ , there is a corresponding coefficient  $\alpha$ . More precisely,  $\alpha_{1,\ell,j,g}$  represents a  
985 gene expression change per unit change of  $x_{1,i,\ell,g}$  for gene  $j$  in sample  $g$ . Note that this coefficient is  
986 the same across all cell types. On the other hand,  $\alpha_{2,\ell,k,j,g}$  represents a gene expression change per  
987 unit change of  $x_{2,i,\ell,g}$  specific to cell type  $k$  in sample  $g$ . Finally,  $\alpha_{2,0,k,j,g}$  represents the intercept  
988 term for gene  $j$  and cell type  $k$  in sample  $g$ . For ease of notation, we will sometimes use  $\alpha_{1,\ell,k,j,g}$  to  
989 equal  $\alpha_{1,\ell,j,g}$  for all  $k$ . Moreover, we will use  $\alpha$  to refer to the joint vector of both  $\alpha_1$  and  $\alpha_2$ . The  
990 parameters  $\alpha$  are estimated by GLAMDE by maximum likelihood. GLAMDE also obtains standard  
991 errors for each coefficient  $\alpha$ . These standard errors are subsequently used for confidence intervals and  
992 hypothesis testing.

### 993 Maximum Likelihood Estimation

994 GLAMDE estimates the parameters of (9) via maximum likelihood estimation. First, we note that  
995 all parameters in the model are independent across samples. As such, we fit the model independently  
996 for each sample, and we now drop the subscript of sample  $g$  for notational convenience. We will  
997 return to the issue of integrating results across multiple samples in *Multiple replicates*. First, the  
998 parameters  $\beta_{i,k}$  and  $\gamma_j$  are estimated by the RCTD algorithm as previously described [24]. We can  
999 accurately estimate cell type proportions and platform effects without being aware of differential spatial

1000 gene expression because differential spatial gene expression is smaller than gene expression differences  
 1001 across cell types. After identifying cell types, GLAMDE estimates gene-specific overdispersion  $\sigma_{\varepsilon,j}$   
 1002 for each gene by maximum likelihood estimation (see *Fitting the overdispersion parameter*). Finally,  
 1003 GLAMDE estimates the parameters  $\alpha_{1,\ell,j}$  and  $\alpha_{2,\ell,k,j}$  by maximum likelihood estimation. For the  
 1004 final key step of estimating  $\alpha$ , we use plugin estimates (denoted by  $\hat{\cdot}$ ) of  $\beta_{i,k}$ ,  $\gamma_j$ , and  $\sigma_\varepsilon$ . After we  
 1005 substitute (10) into (9), we obtain:

$$Y_{i,j} | \varepsilon_{i,j} \sim \text{Poisson} \left\{ N_i \exp \left[ \log \left( \sum_{k=1}^K \hat{\beta}_{i,k} \exp \left( \alpha_{2,0,k,j} + \sum_{\ell=1}^{L_1} x_{1,i,\ell} \alpha_{1,\ell,j} + \sum_{\ell=1}^{L_2} x_{2,i,\ell} \alpha_{2,\ell,k,j} \right) \right) + \hat{\gamma}_j + \varepsilon_{i,j} \right] \right\} \quad (11)$$

$$\varepsilon_{i,j} \sim \text{Normal}(0, \hat{\sigma}_{\varepsilon,j}^2), \quad (12)$$

1006 Now, we provide an algorithm for computing the maximum likelihood estimator of  $\alpha$ . Our likelihood  
 1007 optimization algorithm is a second-order, trust-region based optimization. In brief, we iteratively  
 1008 solve quadratic approximations of the log-likelihood, adaptively constraining the maximum parameter  
 1009 change at each step. Critically, the likelihood is independent for each gene, so separate genes can be  
 1010 run in parallel.

1011 Now, we consider the computation of the maximum likelihood estimator (MLE) of  $\alpha$  for the likeli-  
 1012 hood  $\mathcal{L}(\alpha)$  of observing  $Y_i$  for  $1 \leq i \leq I$ , using the assumption that measurements on separate pixels  
 1013 are independent. We define the predicted counts at pixel  $i$  as  $\bar{\lambda}_i(\alpha)$ , where,

$$\log(\bar{\lambda}_i(\alpha)) := \log \left( N_i \sum_{k=1}^K \hat{\beta}_{i,k} \mu_{i,k} \right) + \hat{\gamma}. \quad (13)$$

1014 From now on, we will drop the constant term  $\hat{\gamma}$ , as it can be equivalently factored into the  $\mu$  intercept  
 1015 term. Next, we can use (9) to compute the likelihood of the GLAMDE model,

$$\mathcal{L}(\alpha) = \sum_{i=1}^I \log P(Y_i | \bar{\lambda}_i(\alpha)) = \sum_{i=1}^I \log Q_{Y_i}(\bar{\lambda}_i(\alpha)), \quad (14)$$

1016 where we have introduced the function  $Q$  to represent the probability, under our Poisson-log-normal  
 1017 sampling model, of observing  $Y_i$  counts given predicted counts  $\lambda_i(\alpha)$ ,

$$Q_\ell(\lambda) \equiv \int_{-\infty}^{\infty} p_{\sigma_\varepsilon}(z) e^{-\lambda e^z} \frac{(e^z \lambda)^\ell}{\ell!} dz, \quad (15)$$

1018 where  $p_{\sigma_\varepsilon}$  is the normal distribution pdf with standard deviation  $\sigma_\varepsilon$ . To optimize our likelihood, we  
 1019 develop a second-order trust-region optimization method [79], in which sequential quadratic approx-  
 1020 imations are optimized within a trust region, whose size is determined adaptively. To do so, we first  
 1021 initialize  $\alpha$  as  $\alpha_0$ , which is set to 0 for intercept terms, and  $-5$  for non-intercept terms. Additionally,  
 1022 we initialize the trust-region width,  $\delta$ , as  $\delta_0 = 0.1$ . At step  $n + 1$  of the algorithm, with previous  
 1023 parameters  $\alpha_n$  and  $\delta_n$ , we make the following quadratic Taylor approximation,  $\tilde{\mathcal{L}}_n$  to  $\mathcal{L}$ ,

$$-\mathcal{L}(\alpha) \approx -\tilde{\mathcal{L}}_n := -\mathcal{L}(\alpha_n) + b(\alpha_n)^T (\alpha - \alpha_n) + \frac{1}{2} (\alpha - \alpha_n)^T A(\alpha_n) (\alpha - \alpha_n), \quad (16)$$

1024 where  $b$  and  $A$  represent the gradient and Hessian of  $-\mathcal{L}$ , respectively, which are computed below. Next,  
 1025 we define  $\alpha_n^*$  as the solution to the following optimization problem of this quadratic approximation  
 1026 over the trust region:

$$\begin{aligned} \min_{\alpha} \quad & b(\alpha_n)^T (\alpha - \alpha_n) + \frac{1}{2} (\alpha - \alpha_n)^T A(\alpha_n) (\alpha - \alpha_n) \\ \text{s.t.} \quad & |\alpha_j - \alpha_{n,j}| \leq \delta_n \quad \text{for } 1 \leq j \leq \text{length}(\alpha) \end{aligned} \quad (17)$$



1027 This quadratic program is solved using the `quadprog` package in R [78]. Next, we define  $\alpha_{n+1}$  as:

$$\alpha_{n+1} := \begin{cases} \alpha_n^*, & \mathcal{L}(\alpha_n^*) - \mathcal{L}(\alpha_n) \geq \gamma(\tilde{\mathcal{L}}_n(\alpha_n^*) - \tilde{\mathcal{L}}_n(\alpha_n)) \\ \alpha_n, & \mathcal{L}(\alpha_n^*) - \mathcal{L}(\alpha_n) < \gamma(\tilde{\mathcal{L}}_n(\alpha_n^*) - \tilde{\mathcal{L}}_n(\alpha_n)), \end{cases} \quad (18)$$

1028 where  $\gamma = 0.1$ . Additionally, the trust region is updated as:

$$\delta_{n+1} := \begin{cases} \beta_{\text{succ}}\delta_n, & \mathcal{L}(\alpha_n^*) - \mathcal{L}(\alpha_n) \geq \gamma(\tilde{\mathcal{L}}_n(\alpha_n^*) - \tilde{\mathcal{L}}_n(\alpha_n)) \\ \beta_{\text{fail}}\delta_n, & \mathcal{L}(\alpha_n^*) - \mathcal{L}(\alpha_n) < \gamma(\tilde{\mathcal{L}}_n(\alpha_n^*) - \tilde{\mathcal{L}}_n(\alpha_n)), \end{cases} \quad (19)$$

1029 where  $\beta_{\text{succ}} = 1.1$  and  $\beta_{\text{fail}} = 0.5$ , which, along with  $\gamma$ , were chosen by a combination of using standard  
 1030 parameter choices [79] and ensuring efficient and stable convergence to local minima. Intuitively, the  
 1031 quadratic approximation  $\tilde{\mathcal{L}}_n$  will only be accurate within a local region, and the trust region is intended  
 1032 to empirically approximate that region. In order to test whether our local approximation is accurate,  
 1033 we check whether the predicted gain in log-likelihood,  $\tilde{\mathcal{L}}_n(\alpha_n^*) - \tilde{\mathcal{L}}_n(\alpha_n)$ , is close to the true gain in  
 1034 log-likelihood,  $\mathcal{L}(\alpha_n^*) - \mathcal{L}(\alpha_n)$ , within a factor of  $\gamma$ . If the local approximation is indeed accurate, the  
 1035 algorithm takes a step, and the trust region is allowed to grow. If not, the algorithm stays put, and the  
 1036 trust region shrinks. This prevents the algorithm from diverging due to poor quadratic approximations.  
 1037 This procedure is repeated until convergence (see *Stopping conditions and convergence*).

### 1038 Gradient and Hessian

1039 In this section, we will derive an expression for the gradient and hessian of  $-\mathcal{L}(\alpha)$ . First, we can  
 1040 calculate the gradient as,

$$\begin{aligned} b(\alpha) = -\nabla L(\alpha) &= -\sum_{i=1}^I \nabla \log Q_{Y_i}(\bar{\lambda}_i(\alpha)) \\ &= -\sum_{i=1}^I \frac{Q'_{Y_i}(\bar{\lambda}_i(\alpha))}{Q_{Y_i}(\bar{\lambda}_i(\alpha))} \nabla \bar{\lambda}_i(\alpha). \end{aligned} \quad (20)$$

1041 Additionally, we have the Hessian,

$$\begin{aligned} A(\alpha) = \text{Hess}(-L(\alpha)) &= -\sum_{i=1}^I \nabla \left( \frac{Q'_{Y_i}(\bar{\lambda}_i(\alpha))}{Q_{Y_i}(\bar{\lambda}_i(\alpha))} \right) (\nabla \bar{\lambda}_i(\alpha))^T - \sum_{i=1}^I \left( \frac{Q'_{Y_i}(\bar{\lambda}_i(\alpha))}{Q_{Y_i}(\bar{\lambda}_i(\alpha))} \right) \nabla^2 \bar{\lambda}_i(\alpha) \\ &= -\sum_{i=1}^I \left( \frac{Q''_{Y_i}(\bar{\lambda}_i(\alpha))}{Q_{Y_i}(\bar{\lambda}_i(\alpha))} - \left( \frac{Q'_{Y_i}(\bar{\lambda}_i(\alpha))}{Q_{Y_i}(\bar{\lambda}_i(\alpha))} \right)^2 \right) (\nabla \bar{\lambda}_i(\alpha)) (\nabla \bar{\lambda}_i(\alpha))^T \\ &\quad - \sum_{i=1}^I \left( \frac{Q'_{Y_i}(\bar{\lambda}_i(\alpha))}{Q_{Y_i}(\bar{\lambda}_i(\alpha))} \right) \nabla^2 \bar{\lambda}_i(\alpha). \end{aligned} \quad (21)$$

1042 We recall the procedure for computing  $Q$  and its derivatives as previously described [24]. What remains  
 1043 is to calculate explicit expressions for  $\bar{\lambda}$  and its derivatives, which we do now. From (10) and (15), we  
 1044 recall the definition of  $\bar{\lambda}_i(\alpha)$ :

$$\bar{\lambda}_i(\alpha) = N_i \sum_{k=1}^K \hat{\beta}_{i,k} \exp \left( \sum_{\ell=1}^{L_2} x_{2,i,\ell} \alpha_{2,\ell,k} + \sum_{\ell=1}^{L_1} x_{1,i,\ell} \alpha_{1,\ell} \right). \quad (22)$$

1045 Next, we calculate the gradient of  $\bar{\lambda}$  with respect to  $\alpha_1$  and  $\alpha_2$  separately:

$$\begin{aligned}\nabla_{\alpha_1} \bar{\lambda}_i(\alpha) &= N_i \sum_{k=1}^K \hat{\beta}_{i,k} \exp \left( \sum_{\ell=1}^{L_2} x_{2,i,\ell} \alpha_{2,\ell,k} + \sum_{\ell=1}^{L_1} x_{1,i,\ell} \alpha_{1,\ell} \right) x_{1,i} = \bar{\lambda}_i(\alpha) x_{1,i}, \\ \nabla_{\alpha_2^{(k)}} \bar{\lambda}_i(\alpha) &= N_i \hat{\beta}_{i,k} \exp \left( \sum_{\ell=1}^{L_2} x_{2,i,\ell} \alpha_{2,\ell,k} + \sum_{\ell=1}^{L_1} x_{1,i,\ell} \alpha_{1,\ell} \right) x_{2,i} = \bar{\lambda}_i^{(k)}(\alpha) x_{2,i},\end{aligned}\tag{23}$$

1046 where we have defined  $\bar{\lambda}_i^{(k)}(\alpha) = N_i \hat{\beta}_{i,k} \exp \left( \sum_{\ell=1}^{L_2} x_{2,i,\ell} \alpha_{2,\ell,k} + \sum_{\ell=1}^{L_1} x_{1,i,\ell} \alpha_{1,\ell} \right)$ . Next, we can com-  
1047 pute the second derivatives:

$$\nabla_{\alpha_1} \nabla_{\alpha_1} \bar{\lambda}_i(\alpha) = \bar{\lambda}_i(\alpha) x_{1,i} x_{1,i}^T, \quad \nabla_{\alpha_2^{(k)}} \nabla_{\alpha_1} \bar{\lambda}_i(\alpha) = \bar{\lambda}_i^{(k)}(\alpha) x_{1,i} x_{2,i}^T,\tag{24}$$

$$\nabla_{\alpha_2^{(k)}} \nabla_{\alpha_2^{(k')}} = \bar{\lambda}_i^{(k)}(\alpha) x_{2,i} x_{2,i}^T \mathbb{I}[k = k'].\tag{25}$$

1048 Finally, notice that all the above expressions, including  $\bar{\lambda}_i$  and  $\bar{\lambda}_i^{(k)}$  across all pixels  $i$ , can be computed  
1049 efficiently using matrix multiplications. Lastly, the Fisher information is computed as a scaled version  
1050 of the Hessian (see *Justification of consistency and asymptotic normality*).

### 1051 Stopping conditions and convergence

1052 The algorithm stops when one of two conditions are satisfied:  $\delta_n < \varepsilon_1$  or  $\tilde{\mathcal{L}}_n(\alpha_n^*) - \tilde{\mathcal{L}}_n(\alpha_n) < \varepsilon_2$  for 6  
1053 consecutive iterations. Default choices are  $\varepsilon_1 = .001$  and  $\varepsilon_2 = .00001$ . Assume that the algorithm stops  
1054 after  $n-1$  iterations and arrives at solution  $\alpha_n$ . Convergence is defined by considering the distance of  $\alpha_n$   
1055 to the optimal solution of  $\tilde{\mathcal{L}}_n$ , which is the maximum step size of the next step of the algorithm. Since  
1056  $\tilde{\mathcal{L}}_n$  is a quadratic function, its maximum can be calculated as  $\alpha^* := \alpha_n - A(\alpha_n)^{-1} b(\alpha_n)$ . Consequently,  
1057  $\alpha_n - \alpha^* = A(\alpha_n)^{-1} b(\alpha_n)$ . For each parameter  $1 \leq i \leq \text{length}(\alpha)$ , we define that parameter  $i$  has  
1058 converged if  $|\alpha_{n,i} - \alpha_i^*| \leq \varepsilon_3$ , where  $\varepsilon_3 = .01$ . Intuitively, for all parameters  $i$  such that  $|\alpha_{n,i} - \alpha_i^*| \leq \varepsilon_3$ ,  
1059 these parameters will change by at most  $\varepsilon_3$  in the next step of the algorithm. Note that it is possible  
1060 for some parameters to converge while others do not. In the most common scenario, consider a case  
1061 in which one cell type has very low gene expression in the gene of interest. In this case, it is possible  
1062 that the parameter controlling the expression of this gene will diverge to  $-\infty$ . As such, this parameter  
1063 doesn't have a practical effect on the model, but it should not prevent the other parameters (of cell  
1064 types with higher expression) from converging. For each cell type, we filter out genes that did not  
1065 converge for downstream analysis. In the multi-region case, for each cell type, we test for differential  
1066 expression among the subset of regions that have converged.

### 1067 Fitting the overdispersion parameter

1068 Here, we describe the procedure for fitting the gene-dependent overdispersion parameter  $\sigma_{\varepsilon,j}$ . This is  
1069 necessary because we found evidence that the overdispersion depends on gene  $j$ , and modeling gene-  
1070 specific overdispersion is necessary for controlling the false-positive rate of GLAMDE. In order to fit a  
1071 gene-dependent overdispersion parameter, we fit GLAMDE with initial overdispersion parameter  $\sigma_\varepsilon$ ,  
1072 which is obtained from the cell type identification step. Next, we use the fitted parameters  $\alpha$  and  
1073 calculate the log-likelihood of GLAMDE for each possible choice of  $\sigma$  (out of a discrete set ranging  
1074 from 0.1 to 2). Because the log-normal distribution has a mean of  $e^{\sigma^2/2}$ , the GLAMDE predicted  
1075 expression values  $\bar{\lambda}$  are scaled by  $e^{-\sigma^2/2}$  to maintain a consistent mean across different values of  $\sigma$ . In  
1076 practice, this decision substantially increases the rate of convergence. After computing log-likelihood  
1077 values for each  $\sigma$ , the best  $\sigma$  is chosen, and the parameters of GLAMDE are re-fit. This procedure is  
1078 repeated until convergence at  $\sigma = \sigma_{\varepsilon,j}$ .



## 1079 Predicted mean and variance of individual data pixel counts

1080 After  $\alpha$  is estimated, we can compute the predicted mean and variance of  $Y_i$ , given  $x_i$ , according to the  
 1081 GLAMDE model. These predictions are used to check whether the observed behavior of data points  
 1082 agrees with the predictions of the GLAMDE model. Rewriting (9),

$$Y_i | \alpha \sim \text{Poisson} \left\{ \text{Lognormal}(\bar{\lambda}_i(\alpha), \sigma_{\varepsilon,j}^2) \right\}. \quad (26)$$

1083 Using properties of the lognormal distribution, we can calculate the mean counts,

$$\mathbb{E}[Y_i | \alpha] = \bar{\lambda}_i(\alpha) e^{\sigma_{\varepsilon,j}^2/2}, \quad (27)$$

1084 as well as the variance of the counts, using the law of total variance,

$$\begin{aligned} \text{Var}[Y_i | \alpha] &= \mathbb{E}[\text{Var}[Y_i | \alpha, \varepsilon_i]] + \text{Var}_{\varepsilon_i}[\mathbb{E}[Y_i | \alpha, \varepsilon_i]] \\ &= \bar{\lambda}_i(\alpha) e^{\sigma_{\varepsilon,j}^2/2} + \bar{\lambda}_i(\alpha)^2 e^{\sigma_{\varepsilon,j}^2} (e^{\sigma_{\varepsilon,j}^2/2} - 1), \end{aligned} \quad (28)$$

1085 where the first part used the equivalence of the mean and variance of the Poisson distribution, and the  
 1086 second part used the variance of the lognormal distribution.

## 1087 Multiple replicates

1088 In order to extend the hypothesis testing framework to the case of multiple replicates, we now recall  
 1089  $\alpha_g$  and  $s_g$  to be the differential expression and standard error for replicate  $g$ , where  $1 \leq g \leq G$ , and  
 1090  $G > 1$  is the total number of replicates. We will consider testing for differential expression for fixed  
 1091 covariate  $\ell$ , cell type  $k$ , and gene  $j$ . In this case, as later derived in (53), the observed estimate  $\hat{\alpha}_{\cdot,\ell,k,j,g}$ ,  
 1092 conditional on  $\alpha$ , follows a univariate normal distribution with standard deviation  $s_{\cdot,\ell,k,j,g}$ :

$$\hat{\alpha}_{\cdot,\ell,k,j,g} | \alpha \sim \text{Normal}(\alpha_{\cdot,\ell,k,j,g}, s_{\cdot,\ell,k,j,g}). \quad (29)$$

1093 We further assume that additional biological and/or technical variation across samples exists, such  
 1094 that each  $\alpha_g$  is normally distributed around a population-level differential expression  $A$ , with standard  
 1095 deviation  $\tau$ :

$$\alpha_{\cdot,\ell,k,j,g} \sim \text{i.i.d. Normal}(A_{\cdot,\ell,k,j}, \tau_{\cdot,\ell,k,j}^2) \quad (30)$$

1096 We estimate  $\tau$  using the method of moments (second moment) on the observed estimate  $\hat{\alpha}$ , obtained  
 1097 independently from each sample:

$$\begin{aligned} \mathbb{E}[\text{V}(\hat{\alpha}_{\cdot,\ell,k,j,1}, \hat{\alpha}_{\cdot,\ell,k,j,2}, \dots, \hat{\alpha}_{\cdot,\ell,k,j,G})] &= \\ &\mathbb{E}[\text{V}((\hat{\alpha}_{\cdot,\ell,k,j,1} - \alpha_{\cdot,\ell,k,j,1}) + \alpha_{\cdot,\ell,k,j,1}, (\hat{\alpha}_{\cdot,\ell,k,j,2} - \alpha_{\cdot,\ell,k,j,2}) + \alpha_{\cdot,\ell,k,j,2}, \dots, \\ &(\hat{\alpha}_{\cdot,\ell,k,j,G} - \alpha_{\cdot,\ell,k,j,G}) + \alpha_{\cdot,\ell,k,j,G})] \\ &= \mathbb{E}[\text{V}((\hat{\alpha}_{\cdot,\ell,k,j,1} - \alpha_{\cdot,\ell,k,j,1}), (\hat{\alpha}_{\cdot,\ell,k,j,2} - \alpha_{\cdot,\ell,k,j,2}), \dots, (\hat{\alpha}_{\cdot,\ell,k,j,G} - \alpha_{\cdot,\ell,k,j,G}))] \\ &+ \mathbb{E}[\text{V}(\alpha_{\cdot,\ell,k,j,1}, \alpha_{\cdot,\ell,k,j,2}, \dots, \alpha_{\cdot,\ell,k,j,G})] \end{aligned} \quad (31)$$

1098 Here, the second step utilizes the independence of  $\hat{\alpha} - \alpha$  and  $\alpha$ . Additionally, we use the finite sample  
 1099 variance function  $\text{V}$  to denote  $\text{V}(x_1, x_2, \dots, x_G) = \frac{1}{G-1} \sum_{g=1}^G (x_g - \bar{x})^2$ , which is an unbiased estimator  
 1100 of the variance of  $x$  if  $x_g$  is an i.i.d. random variable. Consequently, the second term above equals  
 1101  $\tau_{\cdot,\ell,k,j}^2$ . Additionally, since  $\hat{\alpha} - \alpha$  is mean 0, we can use the fact that for mean 0 variables  $y$  that are  
 1102 coordinate-wise independent,  $\mathbb{E}[\text{V}(y_1, y_2, \dots, y_G)] = \frac{1}{G} \sum_{g=1}^G \text{Var}(y_g)$ . Applying this fact to the first  
 1103 term, we obtain,

$$\mathbb{E}[V(\hat{\alpha}_{\cdot,\ell,k,j,1}, \hat{\alpha}_{\cdot,\ell,k,j,2}, \dots, \hat{\alpha}_{\cdot,\ell,k,j,G})] = \mathbb{E}\left[\frac{1}{G} \sum_{g=1}^G (\hat{\alpha}_{\cdot,\ell,k,j,g} - \alpha_{\cdot,\ell,k,j,g})^2\right] + \tau_{\cdot,\ell,k,j}^2 \quad (32)$$

$$= \frac{1}{G} \sum_{g=1}^G s_{\cdot,\ell,k,j,g}^2 + \tau_{\cdot,\ell,k,j}^2, \quad (33)$$

1104 where we have used the GLAMDE standard errors  $s^2$  to estimate the variance of  $\hat{\alpha} - \alpha$ . Consequently,  
1105 we obtain the following method of moments estimator of  $\tau^2$ :

$$\hat{\tau}_{\cdot,\ell,k,j}^2 := V(\hat{\alpha}_{\cdot,\ell,k,j,1}, \hat{\alpha}_{\cdot,\ell,k,j,2}, \dots, \hat{\alpha}_{\cdot,\ell,k,j,G}) - \frac{1}{G} \sum_{g=1}^G s_{\cdot,\ell,k,j,g}^2 \quad (34)$$

1106 Given the above analysis, the estimator is the unbiased method of moments estimator. Since we know  
1107 that  $\tau^2$  is nonnegative, we next modify our estimator to an estimator that dominates the original:

$$\hat{\tau}_{\cdot,\ell,k,j}^2 := \max\left(\left[V(\hat{\alpha}_{\cdot,\ell,k,j,1}, \hat{\alpha}_{\cdot,\ell,k,j,2}, \dots, \hat{\alpha}_{\cdot,\ell,k,j,G}) - \frac{1}{G} \sum_{g=1}^G s_{\cdot,\ell,k,j,g}^2\right], 0\right). \quad (35)$$

1108 We note that the above method of moments estimator (and our overall approach) is similar to the  
1109 widely used DerSimonian-Laird method in meta-analysis [70, 71]. After utilizing the estimate of  $\tau^2$ ,  
1110 we can now compute the estimate and standard error of  $A$ , as follows. Given equations, (29) and (30),  
1111 we have that  $\hat{\alpha}_{\cdot,\ell,k,j,g}$  is distributed independently for  $1 \leq g \leq G$  as:

$$\hat{\alpha}_{\cdot,\ell,k,j,g} \sim \text{Normal}(A_{\cdot,\ell,k,j}, \tau_{\cdot,\ell,k,j}^2 + s_{\cdot,\ell,k,j,g}^2). \quad (36)$$

1112 By the Gauss-Markov theorem for Generalized Least Squares, the best (i.e. minimum variance) unbi-  
1113 ased estimator of  $A$  is:

$$\hat{A}_{\cdot,\ell,k,j} := \frac{\sum_{g=1}^G (\hat{\alpha}_{\cdot,\ell,k,j,g}) / (\tau_{\cdot,\ell,k,j}^2 + s_{\cdot,\ell,k,j,g}^2)}{\sum_{g=1}^G 1 / (\tau_{\cdot,\ell,k,j}^2 + s_{\cdot,\ell,k,j,g}^2)}. \quad (37)$$

1114 We further plugin our estimate  $\hat{\tau}^2$  for  $\tau^2$ , which is an approach called feasible generalized least squares:

$$\hat{A}_{\cdot,\ell,k,j} := \frac{\sum_{g=1}^G (\hat{\alpha}_{\cdot,\ell,k,j,g}) / (\hat{\tau}_{\cdot,\ell,k,j}^2 + s_{\cdot,\ell,k,j,g}^2)}{\sum_{g=1}^G 1 / (\hat{\tau}_{\cdot,\ell,k,j}^2 + s_{\cdot,\ell,k,j,g}^2)}. \quad (38)$$

1115 Finally, the feasible estimate of variance of this estimator (also by the Gauss-Markov theorem) is:

$$\text{Var}(\hat{A}_{\cdot,\ell,k,j}) = \frac{1}{\sum_{g=1}^G 1 / (\hat{\tau}_{\cdot,\ell,k,j}^2 + s_{\cdot,\ell,k,j,g}^2)}. \quad (39)$$

## 1116 Multiple samples and replicates

1117 After developing a hypothesis testing framework for the case of multiple replicates, we now consider the  
1118 extension of this framework to the more complicated study design of multiple biological samples ( $M$   
1119 samples) with multiple replicates per sample ( $G_m$  replicates per sample). In this case, we now model  
1120  $\alpha$  for each sample  $1 \leq m \leq M$  and each replicate  $1 \leq g \leq G_m$  as normally distributed, independently  
1121 for each replicate, with standard deviation  $\tau$ , as follows,

$$\alpha_{\cdot,\ell,k,j,m,g} \sim \text{Normal}(A_{\cdot,\ell,k,j} + \delta_{\cdot,\ell,k,j,m}, \tau_{\cdot,\ell,k,j}^2), \quad (40)$$

1122 where  $\delta$  represents a sample-specific random effect which is itself normally distributed with standard  
1123 deviation  $\Delta$ ,

$$\delta_{\cdot,\ell,k,j,m} \sim_{\text{i.i.d.}} \text{Normal}(0, \Delta_{\cdot,\ell,k,j}^2). \quad (41)$$

1124 Notice that for fixed sample  $m$ , conditional on  $\delta$ , our problem is identical to the multiple replicate  
1125 case above, given a population-mean of  $A_{\cdot,\ell,k,j} + \delta_{\cdot,\ell,k,j,m}$ . Using this reasoning, we take as an estimate  
1126 of  $\tau^2$  the average, across samples, of the estimates of  $\tau^2$  in (35). As we have utilized the variance  
1127 within each sample to obtain an estimate of  $\tau$ , we will next use the variance across samples to estimate  
1128  $\Delta$ . We take (38) and (39) as the value and variance (conditional on  $\delta$ ) respectively of the following  
1129 unbiased estimate  $E$  of  $A_{\cdot,\ell,k,j} + \delta_{\cdot,\ell,k,j,m}$ , which represents the differential expression within sample  
1130  $m$ ,

$$E_{\cdot,\ell,k,j,m} := \frac{\sum_{g=1}^{G_m} (\hat{\alpha}_{\cdot,\ell,k,j,m,g}) / (\hat{\tau}_{\cdot,\ell,k,j}^2 + s_{\cdot,\ell,k,j,m,g}^2)}{\sum_{g=1}^{G_m} 1 / (\hat{\tau}_{\cdot,\ell,k,j}^2 + s_{\cdot,\ell,k,j,m,g}^2)}. \quad (42)$$

1131 Given that  $E_{\cdot,\ell,k,j,m}$  is an unbiased estimate of  $A_{\cdot,\ell,k,j} + \delta_{\cdot,\ell,k,j,m}$ , we recognize that our problem has  
1132 been reduced to the original multiple replicates problem (addressed above), where  $\alpha$  has been replaced  
1133 with  $A + \delta$ ,  $\tau$  has been replaced with  $\Delta$ ,  $\hat{\alpha}$  has been replaced by  $E$ , and  $s^2$  has been replaced by what  
1134 we define as  $S^2$ , the conditional (on  $\delta$ ) variance of  $E$  given in (39),

$$S_{\cdot,\ell,k,j,m}^2 := \frac{1}{\sum_{g=1}^{G_m} 1 / (\hat{\tau}_{\cdot,\ell,k,j}^2 + s_{\cdot,\ell,k,j,m,g}^2)}. \quad (43)$$

1135 As a result of this observation, we can apply a similar derivation as that of (35) to obtain the following  
1136 method of moments estimate of  $\Delta$ ,

$$\hat{\Delta}_{\cdot,\ell,k,j}^2 := \max \left( \left[ \text{Var}(E_{\cdot,\ell,k,j,1}, E_{\cdot,\ell,k,j,2}, \dots, E_{\cdot,\ell,k,j,M}) - \frac{1}{M} \sum_{m=1}^M S_{\cdot,\ell,k,j,m}^2 \right], 0 \right). \quad (44)$$

1137 Continuing our parallel to our previous result, we use the feasible Gauss-Markov estimator of  $A$  derived  
1138 in in (38) and (39),

$$\hat{A}_{\cdot,\ell,k,j} := \frac{\sum_{m=1}^M (E_{\cdot,\ell,k,j,m}) / (\hat{\Delta}_{\cdot,\ell,k,j}^2 + S_{\cdot,\ell,k,j,m}^2)}{\sum_{m=1}^M 1 / (\hat{\Delta}_{\cdot,\ell,k,j}^2 + S_{\cdot,\ell,k,j,m}^2)}. \quad (45)$$

1139 Moreover, using (39), the feasible estimate of variance of this estimator is,

$$\text{Var}(\hat{A}_{\cdot,\ell,k,j}) = \frac{1}{\sum_{m=1}^M 1 / (\hat{\Delta}_{\cdot,\ell,k,j}^2 + S_{\cdot,\ell,k,j,m}^2)}. \quad (46)$$

1140 Therefore, we have derived estimators of population-level differential expression in the case of multiple  
1141 replicates or multiple samples with multiple replicates.

### 1142 Justification of consistency and asymptotic normality of maximum likelihood 1143 estimator of $\alpha$

1144 Since each gene and each sample analyzed independently, we drop the notation of gene  $j$  and sample  
1145  $g$ . First, we consider the joint distribution of all the variables in our model:  $x_i$ ,  $\beta_i$ , and  $Y_i$ . We recall  
1146 that  $x_i$  and  $Y_i$  are observed, and we assume that these variables are generated i.i.d. for each pixel  
1147 ( $1 \leq i \leq n$ , with  $n := I$ ):

$$Z_i := (x_i, \beta_i, Y_i) \stackrel{\text{i.i.d.}}{\sim} P_\alpha, \quad (47)$$

1148 where  $Z_i$  represents the joint random variable and  $P_\alpha(Z_i) = Q(x_i, \beta_i)P_\alpha(Y_i | x, \beta)$ . Here,  $Q$  represents  
 1149 the joint distribution, across pixels, of cell type proportions and covariates, which we assume does  
 1150 not depend on  $\alpha$ . As estimation of  $\alpha$  does not depend on this term, we will ignore this term. The  
 1151 conditional distribution  $P_\alpha(Y_i | x, \beta)$  is precisely the probabilistic model specified by GLAMDE in (9).  
 1152 For this analysis, we treat  $\beta$  as observed and do not consider the uncertainty around the estimation  
 1153 of  $\beta$ , as errors in the estimation of  $\beta$  are expected to be small and independent across pixels.

1154 Due to the specification of GLAMDE, assuming that the columns of  $x$  are linearly independent,  
 1155 identifiability is satisfied. That is,  $P_\alpha \neq P_{\alpha'}$  for any other pair of distinct parameters  $\alpha$  and  $\alpha'$ . It  
 1156 follows from standard asymptotic theory results [80] (using additional regularity conditions including  
 1157 Lipschitz continuity of second derivatives and local convexity of the GLAMDE log-likelihood within  
 1158 a bounded region) that if we let  $\hat{\alpha}_n$  be the MLE estimator on  $n$  pixels, then asymptotic consistency  
 1159 holds:

$$\hat{\alpha}_n \xrightarrow{\text{a.s.}} \alpha. \quad (48)$$

1160 In addition to consistency, asymptotic normality holds as  $n \rightarrow \infty$  [80]:

$$\sqrt{n}(\hat{\alpha}_n - \alpha) \xrightarrow{d} \mathcal{N}(0, I_\alpha^{-1}), \quad (49)$$

1161 where  $I_\alpha$  is defined to be the Fisher information, which can be represented as,

$$I_\alpha = -\mathbb{E}_\alpha[\nabla^2 \log P_\alpha(Y_i | x, \beta)]. \quad (50)$$

1162 In our case, we will use the observed Fisher information  $\hat{I}_\alpha$  to estimate the Fisher information:

$$\hat{I}_\alpha := -\frac{1}{n} \sum_{i=1}^n \nabla^2 \log P_\alpha(Y_i | x, \beta) = \frac{1}{n} A(\alpha), \quad (51)$$

1163 where  $A(\alpha)$ , defined in (16), is the Hessian of the GLAMDE log-likelihood function. Substituting the  
 1164 Hessian into the equation (49) above, we conclude that approximately for large  $n$ ,

$$(\hat{\alpha}_n - \alpha) \sim \mathcal{N}(0, A(\alpha)^{-1}). \quad (52)$$

1165 Next, for a fixed individual cell type  $k$ , gene  $j$ , sample  $g$ , and covariate  $\ell$ , the distribution of  
 1166  $\hat{\alpha}_{\cdot, \ell, k, j, g}$  follows a univariate normal distribution with standard deviation  $s_{\cdot, \ell, k, j, g}$ . According to (49),  
 1167 if we define  $s$  as  $s_{\cdot, \ell, k, j, g} = \sqrt{(I_{\alpha_{j, g}}^{-1})_{\ell, k} / n}$ , we conclude that,

$$\hat{\alpha}_{\cdot, \ell, k, j, g} | \alpha \sim \text{Normal}(\alpha_{\cdot, \ell, k, j, g}, s_{\cdot, \ell, k, j, g}). \quad (53)$$

1168 Thus, we have derived the asymptotic distribution of  $\hat{\alpha}$ , allowing us to compute confidence intervals  
 1169 and perform statistical inference.

## Supplementary Experimental Methods

### Animal Handling

All procedures involving animals at the Broad Institute were conducted in accordance with the US National Institutes of Health Guide for the Care and Use of Laboratory Animals under protocol number 0120-09-16.

### Transcardial Perfusion

C57BL/6J mice were anesthetized by administration of isoflurane in a gas chamber flowing 3% isoflurane for 1 minute. Anesthesia was confirmed by checking for a negative tail pinch response. Animals were moved to a dissection tray and anesthesia was prolonged via a nose cone flowing 3% isoflurane for the duration of the procedure. Transcardial perfusions were performed with ice cold pH 7.4 HEPES buffer containing 110 mM NaCl, 10 mM HEPES, 25 mM glucose, 75 mM sucrose, 7.5 mM MgCl<sub>2</sub>, and 2.5 mM KCl to remove blood from brain and other organs sampled. The appropriate organs were removed and frozen for 3 minutes in liquid nitrogen vapor and moved to -80C for long term storage.

### Tissue Handling

Fresh frozen tissue was warmed to -20 C in a cryostat (Leica CM3050S) for 20 minutes prior to handling. Tissue was then mounted onto a cutting block with OCT and sliced at a 5° cutting angle at 10 μm thickness. Pucks were then placed on the cutting stage and tissue was maneuvered onto the pucks. The tissue was then melted onto the puck by moving the puck off the stage and placing a finger on the bottom side of the glass. The puck was then removed from the cryostat and placed into a 1.5 mL eppendorf tube. The sample library was then prepared as below. The remaining tissue was re-deposited at -80 C and stored for processing at a later date.

### Puck preparation and sequencing

Pucks were prepared as described recently using barcoded beads synthesized in-house on an Akta Oligopilot 10 according to the updated Slide-seqV2 protocol [2]. Pucks were sequenced using a monobase-encoding sequencing-by-ligation approach also described in the updated protocol. We used slide-seq tools for alignment and processing of Slide-seq data.

Pucks were generated using one of two separate bead batches with the oligo sequences listed below:

Batch 1:

5'-

TTT\_PC\_GCCGGTAATACGACTCACTATAGGGCTACACGACGCTCTCCGATCTJJJJJJTCTTCAGCGTCCCGAGAJ  
JJJJJTCNNNNNNNT25

Batch 2:

5'-

TTT\_PC\_GCCGGTAATACGACTCACTATAGGGCTACACGACGCTCTCCGATCTJJJJJJTCTTCAGCGTCCCGAGAJ  
JJJJNNNNNNNVVT30

“PC” designates a photocleavable linker; “J” represents bases generated by split-pool barcoding, such that every oligo on a given bead has the same J bases; “N” represents bases generated by mixing, so every oligo on a given bead has different N bases; and “TX” represents a sequence of X thymidines. “V” represents bases which may contain A, C, G but not T.

### **Slide-seqV2 library preparation**

#### RNA Hybridization:

Pucks in 1.5 mL tubes were immersed in 200  $\mu$ L of hybridization buffer (6x SSC with 2 U/ $\mu$ L Lucigen NxGen RNase inhibitor) for 15 minutes at room temperature to allow for binding of the RNA to the oligos on the beads.

#### First Strand Synthesis

Subsequently, first strand synthesis was performed by incubating the pucks in RT solution for 30 minutes at room temperature followed by 1.5 hours at 52 °C.

#### RT solution:

115  $\mu$ L H<sub>2</sub>O  
40  $\mu$ L Maxima 5x RT Buffer (Thermofisher, EP0751)  
20  $\mu$ L 10 mM dNTPs (NEB N0477L)  
5  $\mu$ L RNase Inhibitor (Lucigen 30281)  
10  $\mu$ L 50  $\mu$ M Template Switch Oligo (Qiagen #339414YCO0076714)  
10  $\mu$ L Maxima H- RTase (Thermofisher, EP0751)

#### Tissue Digestion:

200  $\mu$ L of 2x tissue digestion buffer was then added directly to the RT solution and the mixture was incubated at 37 °C for 30 minutes.

#### 2x tissue digestion buffer:

200 mM Tris-Cl pH 8  
400 mM NaCl  
4% SDS  
10 mM EDTA  
32 U/mL Proteinase K (NEB P8107S)

#### Second Strand Synthesis:

The solution was then pipetted up and down vigorously to remove beads from the surface, and the glass substrate was removed from the tube using forceps and discarded. 200  $\mu$ L of Wash Buffer was then added to the 400  $\mu$ L of tissue clearing and RT solution mix and the tube was then centrifuged for 2 minutes at 3000 RCF. The supernatant was then removed from the bead pellet, the beads were resuspended in 200  $\mu$ L of Wash Buffer, and were centrifuged again. This was repeated a total of three



times. The supernatant was then removed from the pellet. The beads were then resuspended in 200  $\mu$ L of Exol mix and incubated at 37 °C for 50 minutes.

Wash Buffer:

10 mM Tris pH 8.0  
1 mM EDTA  
0.01% Tween-20

Exol mix:

170  $\mu$ L H<sub>2</sub>O  
20  $\mu$ L Exol buffer  
10  $\mu$ L Exol (NEB M0568)

After Exol treatment the beads were centrifuged for 2 minutes at 3000 RCF. The supernatant was then removed from the bead pellet, the beads were resuspended in 200  $\mu$ L of Wash Buffer, and were centrifuged again. This was repeated a total of three times. The supernatant was then removed from the pellet. The pellet was then resuspended in 200  $\mu$ L of 0.1 N NaOH and incubated for 5 minutes at room temperature. To quench the reaction, 200  $\mu$ L of Wash Buffer was added and beads were centrifuged for 2 minutes at 3000 RCF. The supernatant was then removed from the bead pellet, the beads were resuspended in 200  $\mu$ L of Wash Buffer, and were centrifuged again. This was repeated a total of three times. Second Strand Synthesis was then performed on the beads by incubating the pellet in 200  $\mu$ L of Second Strand Mix at 37 °C for 1 hour.

Second Strand Synthesis mix:

133  $\mu$ L H<sub>2</sub>O  
40  $\mu$ L Maxima 5x RT Buffer  
20  $\mu$ L 10 mM dNTPs  
2  $\mu$ L 1 mM dN-SMRT oligo  
5  $\mu$ L Klenow Enzyme (NEB M0210)

After Second Strand Synthesis, 200  $\mu$ L of Wash Buffer was added and the beads were centrifuged for 2 minutes at 3000 RCF. The supernatant was then removed from the bead pellet, the beads were resuspended in 200  $\mu$ L of Wash Buffer, and were centrifuged again. This was repeated a total of three times.

Library Amplification:

200  $\mu$ L of water was then added to the bead pellet and the beads were centrifuged for 2 minutes at 3000 RCF. The supernatant was then removed from the bead pellet and the beads were resuspended in 50  $\mu$ L of library PCR mix and moved into a 200  $\mu$ L PCR strip tube. PCR was then performed as outlined below:

Library PCR mix:

22  $\mu$ L H<sub>2</sub>O  
25  $\mu$ L of Terra Direct PCR mix Buffer (Takara Biosciences 639270)  
1  $\mu$ L of Terra Polymerase (Takara Biosciences 639270)  
1  $\mu$ L of 100  $\mu$ M Truseq PCR primer (IDT)  
1  $\mu$ L of 100  $\mu$ M SMART PCR primer (IDT)

PCR program:

95 °C 3 minutes

4 cycles of:

98 °C 20 seconds

65 °C 45 seconds

72 °C 3 minutes

9 cycles of:

98 °C 20 seconds

67 °C 20 seconds

72 °C 3 minutes

Then:

72 °C 5 minutes

Hold at 4 °C

PCR cleanup and Nextera Tagmentation:

Samples were cleaned with Ampure XP (Beckman Coulter A63880) beads in accordance with manufacturer's instructions at a 0.6x bead/sample ratio (30 µL of beads to 50 µL of sample) and resuspended in 50 µL of water. The cleanup procedure was repeated, this time resuspending in a final volume of 10 µL. 1 µL of the library was quantified on an Agilent Bioanalyzer High sensitivity DNA chip (Agilent 5067-4626). Then, 600 pg of cDNA was taken from the PCR product and prepared into Illumina sequencing libraries through tagmentation using the Nextera XT kit (Illumina FC-131-1096). Tagmentation was performed according to manufacturer's instructions and the library was amplified with primers Truseq5 and N700 series barcoded index primers. The PCR program was as follows:

PCR program:

72 °C for 3 minutes

95 °C for 30 seconds

12 cycles of:

95 °C for 10 seconds

55 °C for 30 seconds

72 °C for 30 seconds

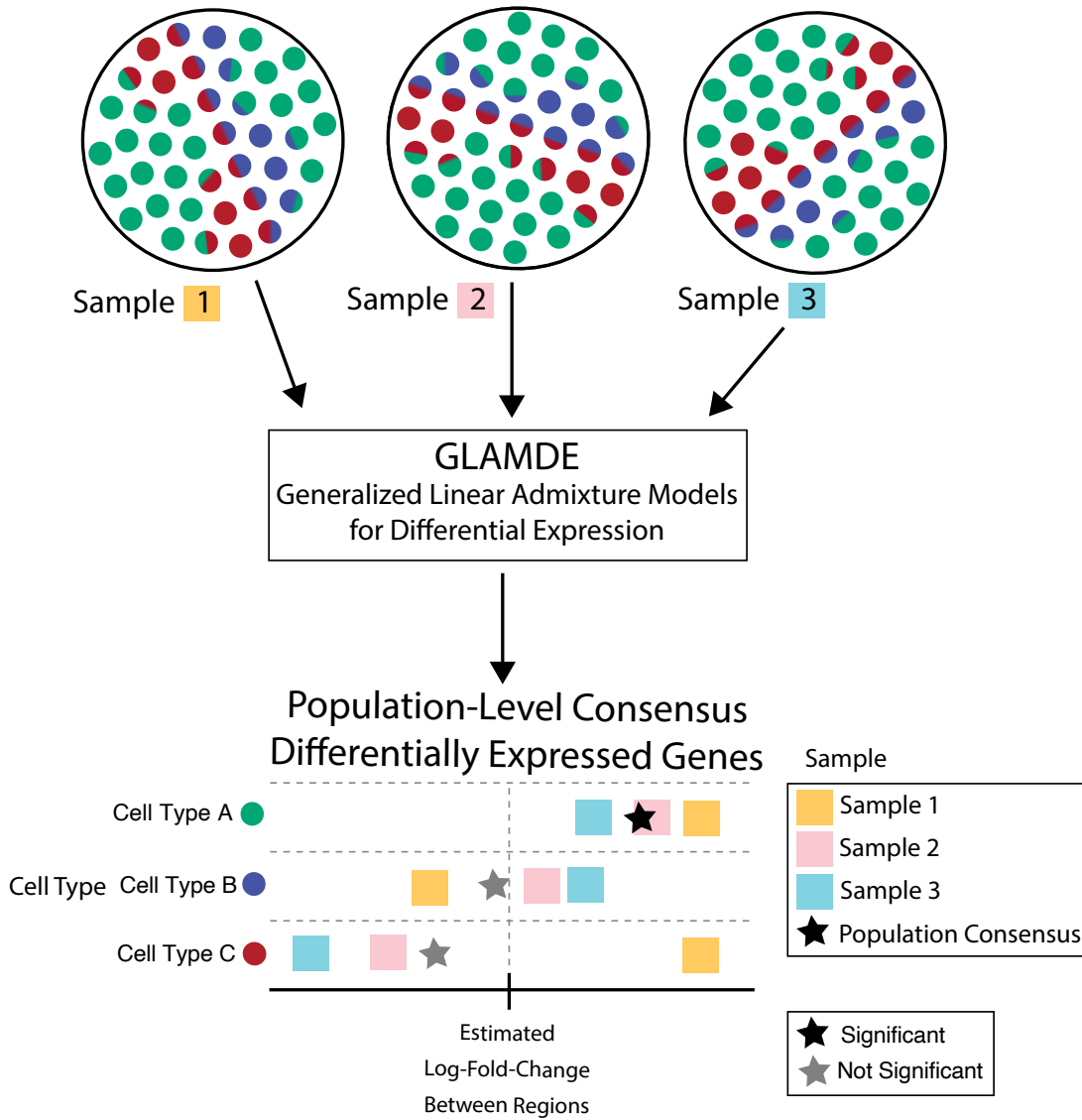
72 °C for 5 minutes

Hold at 4 °C

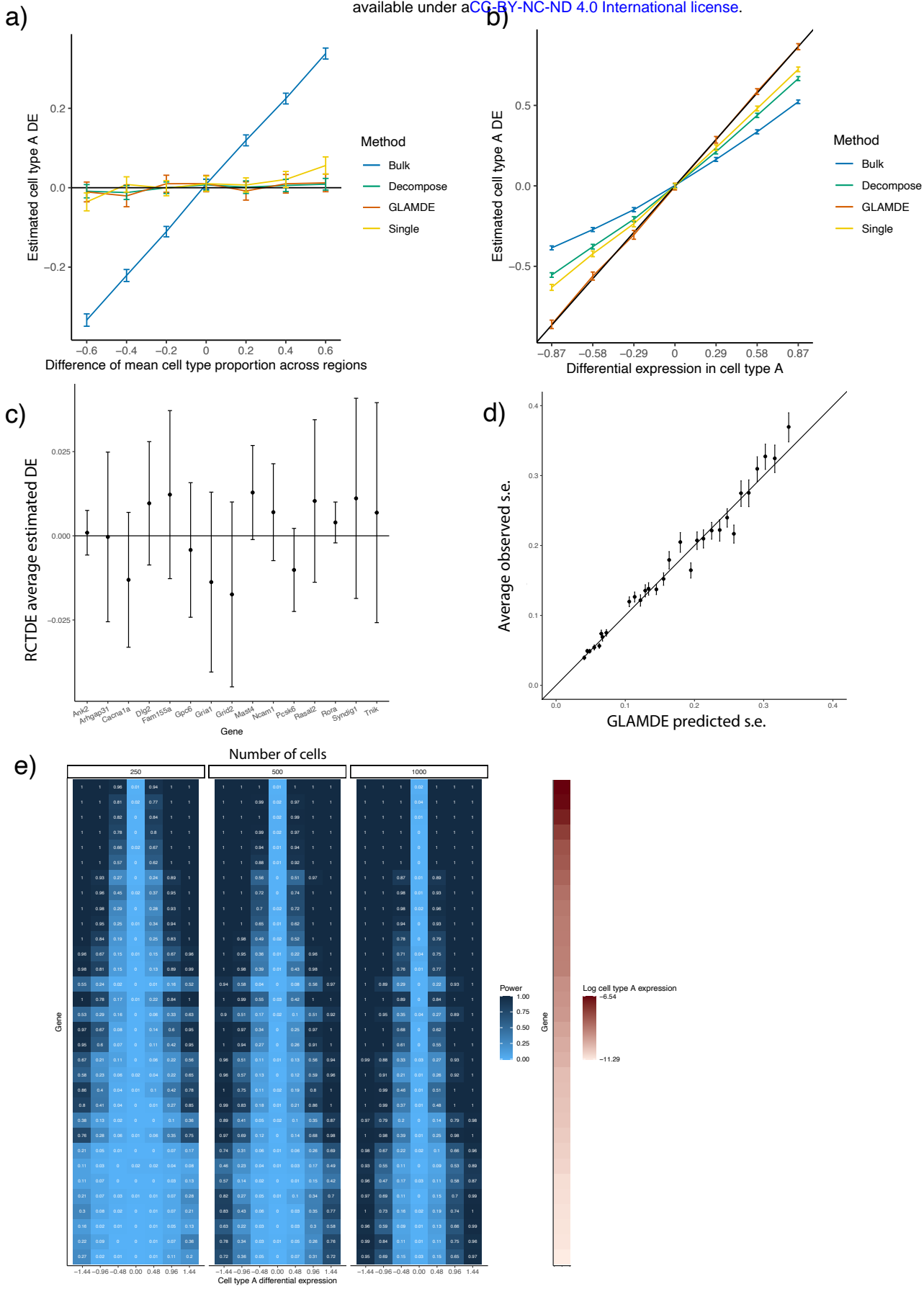
Samples were cleaned with Ampure XP (Beckman Coulter A63880) beads in accordance with manufacturer's instructions at a 0.6x bead/sample ratio (30 µL of beads to 50 µL of sample) and resuspended in 10 µL of water. 1 µL of the library was quantified on an Agilent Bioanalyzer High sensitivity DNA chip (Agilent 5067-4626). Finally, the library concentration was normalized to 4 nM for sequencing. Samples were sequenced on the Illumina NovaSeq S2 flowcell 100 cycle kit with 12 samples per run (6 samples per lane) with the read structure 44 bases Read 1, 8 bases i7 index read, 50 bases Read 2. Each puck received approximately 200-400 million reads, corresponding to 3,000-5,000 reads per bead.

## 1170 **Supplementary Figures**

## Multiple replicates/samples



1171       Supplementary figure 1: GLAMDE can integrate results from multiple samples to form a robust  
1172 estimate of population-level consensus differentially-expressed genes.





1173 Supplementary figure 2: In simulated data, GLAMDE provides unbiased estimates of cell type-  
1174 specific differential expression, with calibrated  $p$ -values.

1175 All: GLAMDE was tested on a dataset of simulated mixtures of single cells from a single-nucleus  
1176 RNA-seq cerebellum dataset.

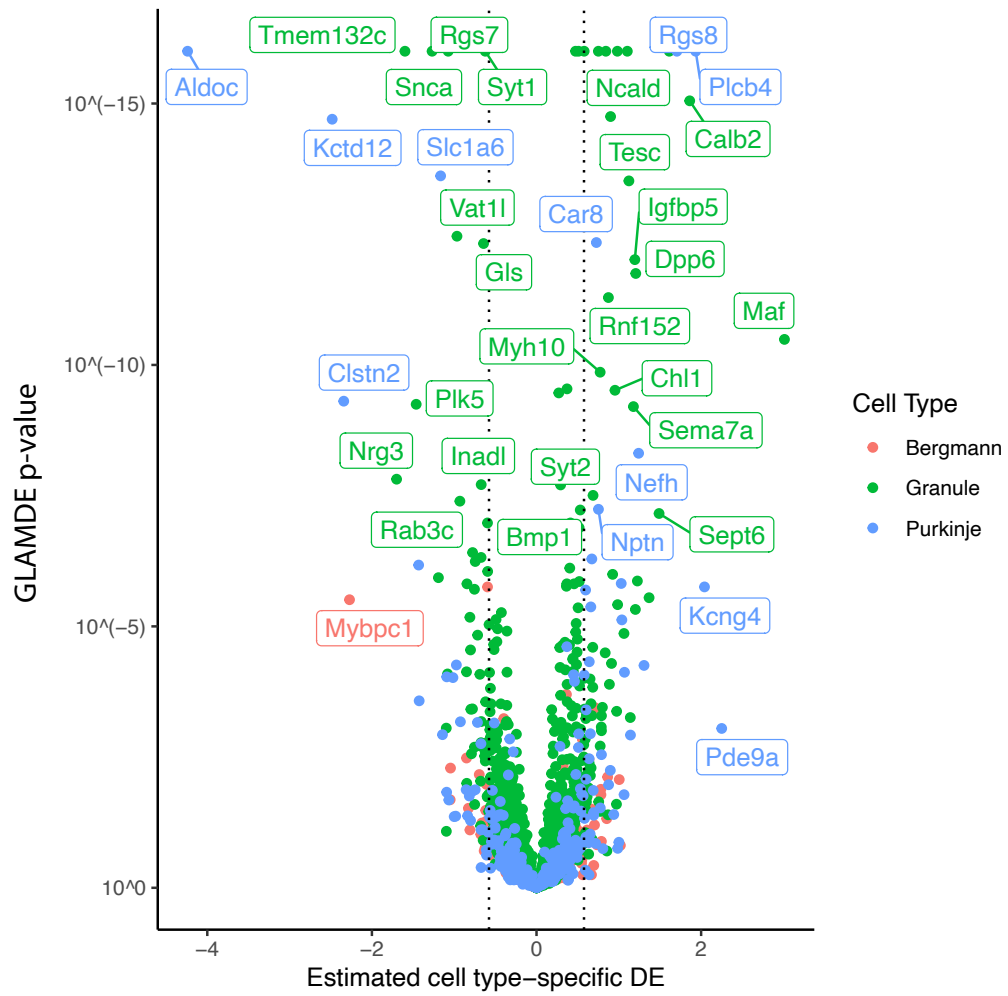
1177 (a) Mean estimated cell type A *Astn2* DE (differential expression) across two regions as a function of  
1178 the difference in mean cell type proportion across regions. Ground truth 0 spatial DE is simulated,  
1179 and average of ( $n = 100$ ) estimates is shown, along with standard errors. Black line represents  
1180 ground truth 0 DE (cell type B). Four methods are shown: *Bulk*, *Decompose*, *Single*, and *GLAMDE*  
1181 (see *Methods* for details).

1182 (b) Same as (a) for *Nrxn3* cell type A differential gene expression as a function of DE in cell type A,  
1183 where *Nrxn3* is simulated to have DE within cell type A but no DE in cell type B. Ground truth  
1184 identity line shown.

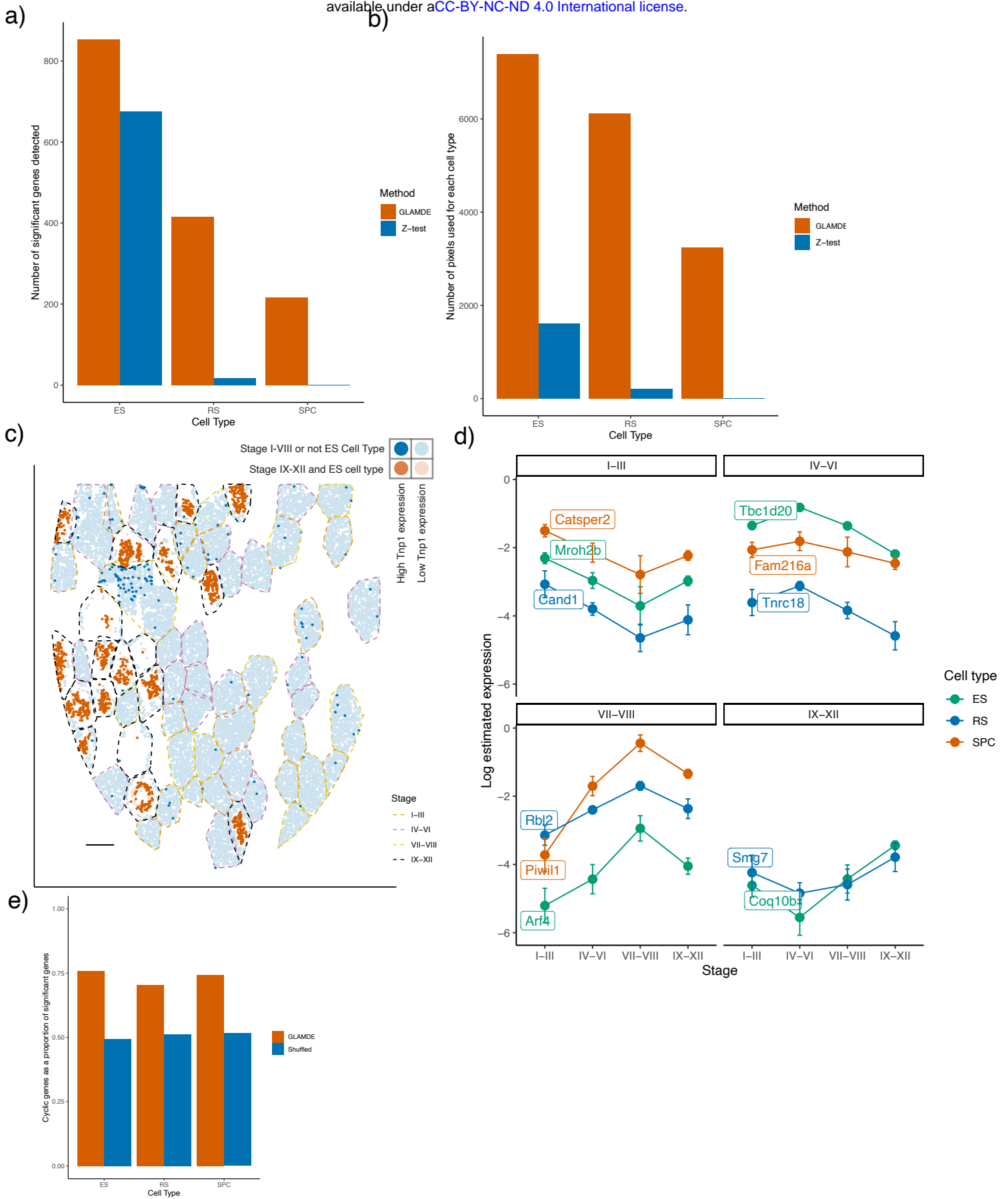
1185 (c) GLAMDE mean estimated cell type B differential expression as a function of gene (average over  
1186  $n = 500$  replicates, with confidence intervals shown). Ground truth line (0 DE) is shown, and each  
1187 condition used a different gene (out of 15 total genes).

1188 (d) Average measured standard error of GLAMDE estimates for each bin of GLAMDE predicted  
1189 standard error.

1190 (e) Statistical power (FPR = 0.01) as a function of gene (y-axis), cell type A DE (x-axis), and number  
1191 of cells (table number). Genes are sorted by cell type A expression (shown on right in log2 counts  
1192 per 1).



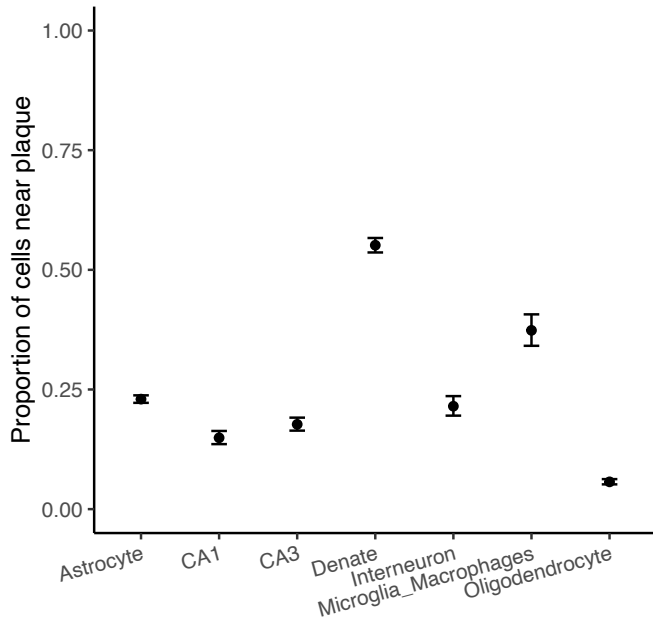
1193       Supplementary figure 3: Volcano plot of GLAMDE log<sub>2</sub> differential expression results for cerebellum  
1194 Slide-seq across three replicates, with positive values representing enrichment in the anterior region  
1195 vs. the nodulus. Color represents cell type, and a subset of significant genes are labeled. Dotted lines  
1196 represents GLAMDE fold-change cutoff at 1.5.



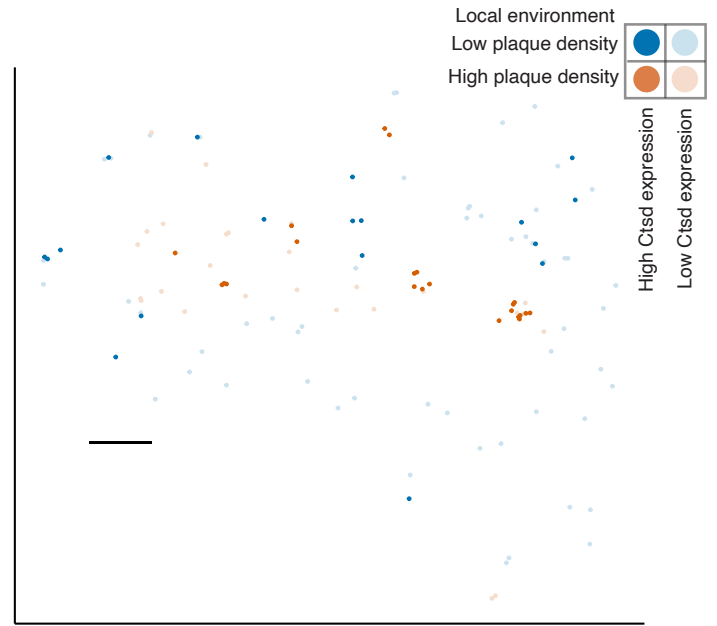
1197 Supplementary figure 4: On the Slide-seq testes, GLAMDE achieves increased power in the presence  
1198 of cell type mixtures to discover tubule stage-specific genes and cyclic genes.

- 1199 (a) Number of significant genes detected, for each cell type, by GLAMDE or the Z-test method.
- 1200 (b) Number of pixels used, for each cell type, to fit the GLAMDE or Z-test model.
- 1201 (c) Spatial plot of *Tnp1*, a gene identified by GLAMDE to be differentially expressed in stage IX-XII of  
1202 cell type ES. Red represents the pixels of cell type ES within stage IX-XII, whereas blue represents  
1203 pixels of another cell type or region. Bold points represent pixels expressing *Tnp1* at a level of at  
1204 least 7.5 counts per 500. Scale bar represents 250 microns.
- 1205 (d) For each cell type, genes identified using GLAMDE results to be cyclic. Panels, indexed by tubule  
1206 stage, contain cyclic genes whose peak estimated expression is at that stage. Error bars represent  
1207 confidence intervals.
- 1208 (e) Proportion of genes categorized as cyclic (using GLAMDE fits), compared to proportion that  
1209 would be categorized as cyclic if tubule stages were shuffled.

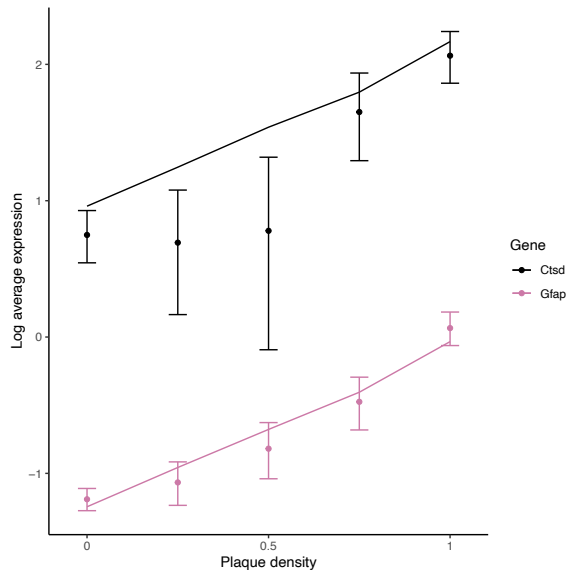
a)



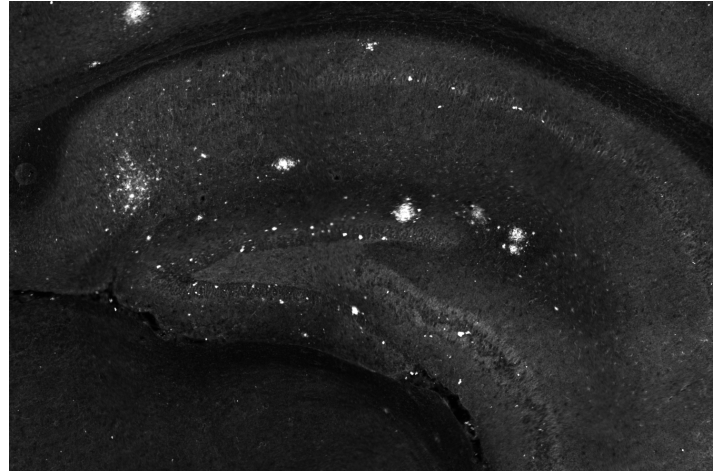
b)



c)



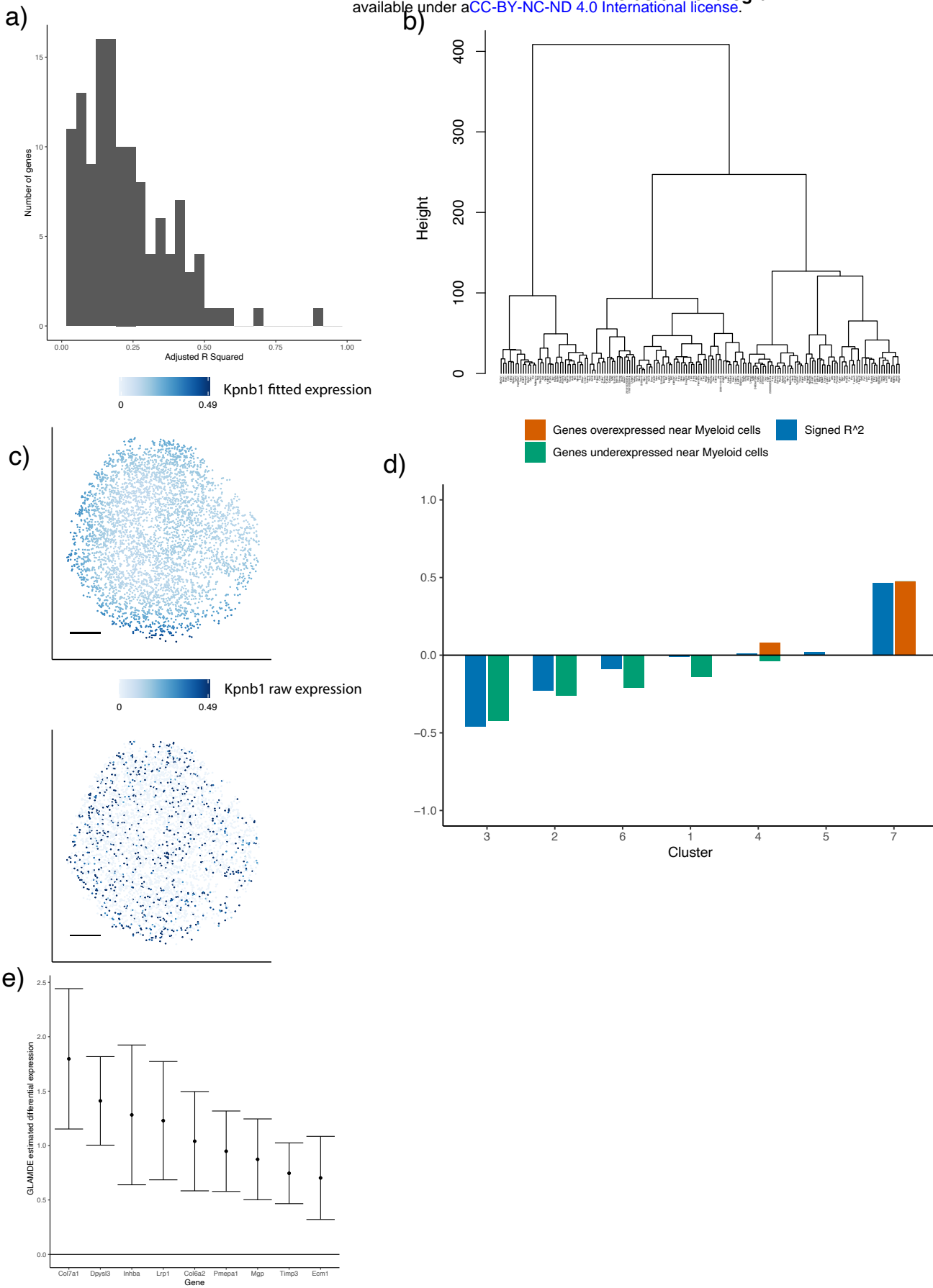
d)





1210 Supplementary figure 5: On the Slide-seq Alzheimer's hippocampus, GLAMDE identifies genes  
1211 whose expression depends on  $A\beta$  plaque density.

- 1212 (a) The proportion of cells, for each cell type, that localize in a high plaque density area.
- 1213 (b) Spatial visualization of *Ctsd*, whose expression within astrocytes was identified by GLAMDE to  
1214 depend on plaque density. Red represents the astrocytes in high plaque density areas, whereas blue  
1215 represents astrocytes in regions of low plaque density. Bold points represent astrocytes expressing  
1216 *Ctsd* at a level of at least 3 counts per 500. Scale bar is 250 microns.
- 1217 (c) Log average expression of genes *Ctsd* and *Gfap*, which were identified to be significantly differ-  
1218 entially expressed by GLAMDE for microglia/macrophages and astrocyte cell types, respectively.  
1219 Single cell type pixels are binned according to plaque density, and points represent raw data av-  
1220 erages while lines represents GLAMDE predictions and error bars around points represent  $\pm 1.96$   
1221 s.d. (*Supplementary Methods*).
- 1222 (d) Antibody stain of  $A\beta$  plaque in adjacent hippocampus section. This image is subsequently trans-  
1223 formed to calculate a covariate for GLAMDE.



1224 Supplementary figure 6: on the Slide-seq mouse tumor, GLAMDE identifies differentially expressed  
1225 genes within tumor cells.

1226 (a) Histogram, across genes identified to be significantly DE within tumor cells by nonparametric  
1227 GLAMDE, of adjusted  $R$ -squared, which is defined as the proportion of variance, not due to  
1228 sampling noise, explained by the GLAMDE model.

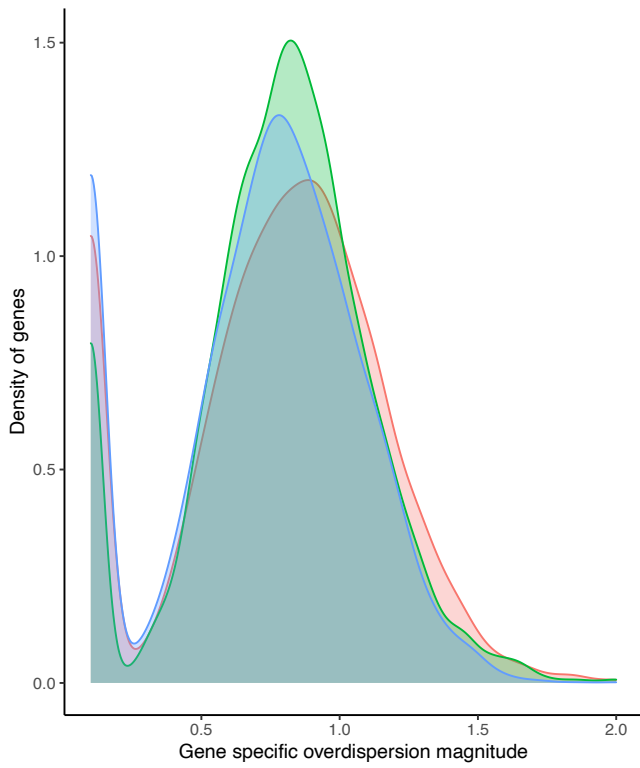
1229 (b) Dendrogram of hierarchical clustering of ( $n = 162$  significant genes) GLAMDE's fitted smooth  
1230 spatial patterns.

1231 (c) Spatial plot in tumor cells of *Kpnb1*, a *Myc*-target gene identified to be differentially expressed by  
1232 nonparametric GLAMDE. Top shows GLAMDE fitted expression, while bottom shows observed  
1233 expression in counts per 500. Scale bars are 250 microns.

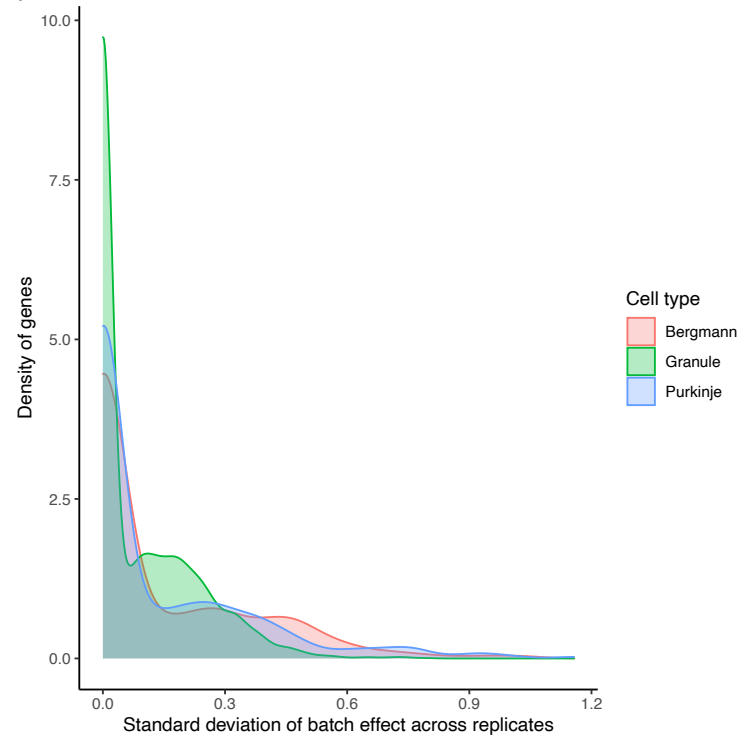
1234 (d) For each cluster of spatially-varying genes, the proportion of genes identified by hypothesis-driven  
1235 GLAMDE to be over- or under-expressed near myeloid cells. This proportion is plotted alongside  
1236 the squared correlation of the cluster to the density of myeloid cells.

1237 (e) GLAMDE estimated differential expression and 95% confidence intervals of 9 genes from the  
1238 epithelial-mesenchymal transition (EMT) pathway identified to be significant.

a)



b)



1239       Supplementary Figure 7: GLAMDE estimated variance parameters on the Slide-seq cerebellum  
1240 data.

1241 (a) Density plot, over genes, of overdispersion standard deviation,  $\sigma_\epsilon$ , for each of three Slide-seq  
1242 replicates.

1243 (b) Density plot, over genes, of GLAMDE estimated batch effect standard deviation,  $\tau$ , for each of  
1244 the Bergmann, granule, and Purkinje cerebellum cell types.